Monthly Notices
of the
ROYAL ASTRONOMICAL SOCIETY

MNRAS **463,** 1844–1864 (2016)
Advance Access publication 2016 August 4

doi:10.1093/mnras/stw1936

A path towards understanding the rotation–activity relation of M dwarfs with K2 mission, X-ray and UV data

B. Stelzer,[1★] M. Damasso,[2] A. Scholz[3] and S. P. Matt[4]

[1]*INAF - Osservatorio Astronomico di Palermo, Piazza del Parlamento 1, I-90134 Palermo, Italy*
[2]*INAF - Osservatorio Astrofisico di Torino, via Osservatorio 20, I-10025 Pino Torinese, Italy*
[3]*SUPA School of Physics & Astronomy, University of St. Andrews, North Haugh, St. Andrews KY 16 9SS, UK*
[4]*Department of Physics and Astronomy, University of Exeter, Physics Building, Stocker Road, Exeter EX4 4QL, UK*

Accepted 2016 August 2. Received 2016 August 1; in original form 2016 March 22

ABSTRACT

We study the relation between stellar rotation and magnetic activity for a sample of 134 bright, nearby M dwarfs observed in the *Kepler* Two-Wheel (K2) mission during campaigns C0–C4. The K2 light curves yield photometrically derived rotation periods for 97 stars (79 of which without previous period measurement), as well as various measures for activity related to cool spots and flares. We find a clear difference between fast and slow rotators with a dividing line at a period of ∼10 d at which the activity level changes abruptly. All photometric diagnostics of activity (spot cycle amplitude, flare peak amplitude and residual variability after subtraction of spot and flare variations) display the same dichotomy, pointing to a quick transition between a high-activity mode for fast rotators and a low-activity mode for slow rotators. This unexplained behaviour is reminiscent of a dynamo mode-change seen in numerical simulations that separates a dipolar from a multipolar regime. A substantial number of the fast rotators are visual binaries. A tentative explanation is accelerated disc evolution in binaries leading to higher initial rotation rates on the main sequence and associated longer spin-down and activity lifetimes. We combine the K2 rotation periods with archival X-ray and UV data. X-ray, FUV and NUV detections are found for 26, 41, and 11 stars from our sample, respectively. Separating the fast from the slow rotators, we determine for the first time the X-ray saturation level separately for early- and for mid-M stars.

Key words: stars: activity – stars: flare – stars: late-type – stars: rotation – ultraviolet: stars – X-rays: stars.

1 INTRODUCTION

Together with convection, rotation is the main driver of stellar dynamos and ensuing magnetic activity phenomena (e.g. Kosovichev, de Gouveia Dal Pino & Yan 2013). In a feedback mechanism, magnetic fields are responsible for the spin-evolution of stars; during part of the pre-main-sequence phase the magnetic field couples the star to its accretion disc dictating angular momentum transfer (Bouvier et al. 2014) and during the main-sequence phase magnetized winds remove angular momentum leading to spin-down (Kawaler 1988; Matt et al. 2015). Rotation and magnetic fields are, therefore, intimately linked and play a fundamental role in stellar evolution.

Magnetic field strength and topology can be measured through Zeeman broadening and polarization, respectively. Collecting the required optical high-resolution (polarimetric) spectroscopic observations is time-consuming, and each of these techniques can be applied only to stars with a limited range of rotation rates (e.g. Donati & Landstreet 2009; Vidotto et al. 2014). However, how the stellar dynamo and the spin-evolution are linked can be addressed by measuring both magnetic activity and rotation rate across evolutionary time-scales. While the activity–age relation is a proxy for the evolution of the stellar dynamo, the rotation–age relation discriminates between models of angular momentum evolution.

In a seminal work by Skumanich (1972), the age decay of both activity and rotation of solar-type stars was established by extrapolating between the age of the oldest known open cluster (600 Myr) and the Sun (4.5 Gyr). Unfortunately, stellar ages are notoriously difficult to assess. Therefore, the direct relation between rotation and activity – observed first some decades ago (e.g. Pallavicini et al. 1981; Vilhu 1984) – has widely substituted studies which involve age-estimates. The early works cited above have used spectroscopic measurements as measure for stellar rotation ($v \sin i$), and carry intrinsic ambiguities related to the unknown inclination angle of the stars. Stellar rotation rates are best derived from the periodic brightness variations induced by cool star-spots moving across the line of sight, which can be directly associated with the rotation period. In more recent studies of the rotation–activity connection,

★E-mail: stelzer@astropa.unipa.it

photometrically measured rotation periods have proven more useful than $v \sin i$ (e.g. Pizzolato et al. 2003; Wright et al. 2011). Especially, for M dwarfs 'saturation' sets in at relatively small values of $v \sin i$ due to their small radii and it is hard to probe the slow-rotator regime with spectroscopic rotation measurements.

Theory predicts a qualitative change of the dynamo mechanism at the transition into the fully convective regime (SpT $\sim$ M3; Stassun et al. 2011). Fully convective stars lack the tachocline in which solar-like $\alpha\Omega$-dynamos originate. Alternative field generation mechanisms must be at work: a turbulent dynamo was proposed by Durney, De Young & Roxburgh (1993) but it is expected to generate only small-scale fields, in contrast to recent results from Zeeman–Doppler imaging (ZDI) which have shown evidence for large-scale dipolar fields in some fully convective stars (Morin et al. 2008, 2010). Current studies of field generation in the fully convective regime are, therefore, concentrating on α^2-dynamos (Chabrier & Küker 2006). While rotation has no influence on turbulent dynamo action, it is considered an important ingredient of mean-field α^2-dynamos. This attributes studies of the rotation dependence of magnetic activity across the M spectral type (SpT) range a crucial meaning for understanding fully convective dynamos. Moreover, while improved spin-down models based on stellar wind simulations have been developed for solar-type stars (Gallet & Bouvier 2013), angular momentum evolution models of M stars are still controversial (Reiners & Mohanty 2012). Therefore, for the most abundant type of stars in our Galaxy, both the characteristics of the stellar dynamo and the angular momentum evolution are still widely elusive.

Rotation–activity studies have been presented with different diagnostics for activity, the most frequently used ones being Hα and X-ray emission. While Hα measurements are available for larger samples, especially thanks to surveys such as the *Sloan Digital Sky Survey* (SDSS; e.g. West et al. 2004), X-ray emission was shown to be more sensitive to low activity levels in M dwarfs (Stelzer et al. 2013). The samples for the most comprehensive rotation–activity studies involving X-ray data have been assembled from a literature compilation, providing a large number of stars, at the expense of homogeneity. Wright et al. (2011) discuss a sample of more than 800 late-type stars (SpT FGKM). However, the rotation–activity relation is not studied separately for M stars, possibly due to a strong bias towards X-ray luminous stars which affects especially the M stars as seen from their fig. 5. Overall, the lack of unbiased overlapping samples with known rotation period and X-ray activity level has left the X-ray–rotation relation of M stars nearly unconstrained (see bottom-right panels of figs 5 and 6 in Pizzolato et al. 2003). Studies with optical emission lines (Hα, Ca II H&K) as activity indicator have for convenience mostly been coupled with $v \sin i$ as rotation measure because both parameters can be obtained from the same set of spectra (Browning et al. 2010; Reiners, Joshi & Goldman 2012). Only lately has it become possible to combine Hα data with photometrically measured M star rotation periods, since a larger sample of periods have become available from ground-based planet transit search programmes (West et al. 2015).

M dwarfs have not yet reached a common rotational sequence even at Gyr-ages, suggesting weaker winds and longer spin-down time-scales as compared to solar-like stars (Irwin et al. 2011). The old and slowly rotating M dwarfs generally have low variability amplitudes resulting from reduced spot coverage and long rotation periods (up to months). From the ground, significant numbers of field M dwarf rotation periods have recently been measured (Newton et al. 2016). However, the sample of their study comprises only very low mass stars ($R_* \leq 0.33\,R_\odot$) and seems to be incomplete in terms of the period detection efficiency (Irwin et al. 2011). The *Kepler* mission (Borucki et al. 2010) with its ability to provide high-precision, long and uninterrupted photometric light curves has led to the detection of rotation periods in >2000 field M dwarfs (McQuillan, Aigrain & Mazeh 2013; Nielsen et al. 2013; McQuillan, Mazeh & Aigrain 2014), a multiple of the number known before. Interesting findings of this *Kepler*-study are (i) the evidence for a bimodal distribution of rotation periods for M dwarfs with $P_{\rm rot} = 0.4$–70 d and (ii) the fact that the envelope for the slowest observed rotation periods shifts towards progressively larger periods for stars with mass below $\sim 0.5\,M_\odot$. How these features in the rotational distribution are connected to stellar activity has not yet been examined. Most of the *Kepler* stars are too distant for detailed characterization in terms of magnetic activity diagnostics. However, the *Kepler* Two-Wheel (K2) mission is ideally suited to study both rotation and activity for nearby M stars.

Since 2014 March, with its two remaining reaction wheels, the *Kepler* spacecraft is restricted to observations in the ecliptic plane changing the pointing direction every $\sim$80 d (Howell et al. 2014). With special data processing correcting for the spacecraft's pointing drift, the photometric precision of K2 is similar to that achieved by the preceding fully functional *Kepler* mission (Vanderburg & Johnson 2014). A great number of field M dwarfs have been selected as K2 targets with the goal of detecting planet transits. Several lists of planet candidates have already been published (e.g. Foreman-Mackey et al. 2015; Montet et al. 2015; Vanderburg et al. 2016), and some interesting planet systems have already been validated, including objects from the target list of this study (see Section 7.8).

In our programme to study the M star rotation–activity connection, we limit the sample to nearby, bright M stars which provide the largest signal to noise in the K2 light curves and are most likely to be detectable at the high energies that are the best probes of magnetic activity. We derive from the K2 mission data both rotation periods and various diagnostics of magnetic activity, and we combine this with X-ray and UV activity from past and present space missions (*ROSAT*, *XMM–Newton*, *GALEX*). As mentioned above, X-ray wavelengths have proven to be more sensitive to low activity levels in M dwarfs than optical emission lines. Moreover, both X-rays and UV photons are known to have a strong impact on close-in planets, providing another motivation for characterizing the high-energy emission of these stars. Given the high occurrence rate of terrestrial planets in the habitable zone of M dwarfs ($\sim$50 per cent according to Kopparapu 2013), a substantial number of the stars we survey may soon be found to host potentially habitable worlds.

The importance of stellar magnetic activity for exoplanet studies is twofold. First, star-spots and chromospheric structures introduce noise in measured radial velocity (RV) curves, so-called RV 'jitter', which depends strongly on the properties of the spots (Andersen & Korhonen 2015). The spectra collected to perform RV measurements can also be used to model star-spots (see e.g. Donati et al. 2015). However, since it is an impossible task to measure the spot distribution for every potentially interesting star, relations between star-spot characteristics and other activity diagnostics such as UV or X-ray emission – if applied to statistical samples – can provide useful estimates of the expected RV noise. Secondly, as mentioned above, the stellar X-ray and UV emission is crucial for the evolution and the photochemistry of planet atmospheres. While the magnetic activity of the star may erode the atmospheres of planets formed in close orbits (e.g. Penz & Micela 2008), it may by the same effect remove the gaseous envelopes of planets migrated inwards from beyond the snow line and render them habitable (Luger et al. 2015). Until recently, photochemical models for planets around

Table 1. Target list for K2 Campaign C0–C4 with stellar parameters.

EPIC ID	Campaign	CNS-name	K_p (mag)	V (mag)	J (mag)	K_s (mag)	d (pc)	M_* ($M_\odot$)	R_* ($R_\odot$)	$\log L_{bol}$ ($L_\odot$)	T_{eff} (K)	SpT
202059188[a]	C0		14.70	14.32 ± 0.05	9.88 ± 0.02	9.04 ± 0.02	22.0	0.27 ± 0.01	0.27 ± 0.01	-2.13 ± 0.04	3181 ± 80	M4.5
202059192	C0		13.10	13.09 ± 0.02	9.99 ± 0.02	9.15 ± 0.02	59.9	0.59 ± 0.01	0.56 ± 0.02	-1.23 ± 0.03	3712 ± 80	M1.0
202059193	C0		12.50	12.42 ± 0.03	9.54 ± 0.02	8.71 ± 0.02	57.2	0.65 ± 0.02	0.63 ± 0.02	-1.08 ± 0.03	3835 ± 82	M0.0
202059195	C0	G 103-029	14.70	14.18 ± 0.06	9.95 ± 0.02	9.07 ± 0.02	25.9	0.31 ± 0.01	0.31 ± 0.01	-1.99 ± 0.05	3306 ± 81	M4.0
202059198	C0		11.60	11.62 ± 0.02	8.48 ± 0.06	7.65 ± 0.02	29.2	0.58 ± 0.02	0.55 ± 0.02	-1.26 ± 0.05	3724 ± 99	M1.0
202059199	C0	LP 420-6	12.60	12.60 ± 0.02	9.06 ± 0.02	8.22 ± 0.03	28.6	0.47 ± 0.01	0.45 ± 0.02	-1.53 ± 0.03	3533 ± 83	M2.5
202059203	C0	LP 362-257	14.10	13.64 ± 0.03	9.71 ± 0.02	8.81 ± 0.02	28.5	0.38 ± 0.01	0.37 ± 0.01	-1.79 ± 0.03	3414 ± 79	M3.0

[a]Potential contamination by companion star in binary (see Appendix B).
[b]M_{Ks} slightly outside the range of calibrated values (see the text in Section 3).
[c]This star (Gl 852B) is not considered further because we assign the rotation and activity to the primary (Gl 852A) in the unresolved binary.
The full table is available in the electronic edition of the journal.

M dwarfs relied exclusively on the observed UV properties of a single strongly active star, AD Leo (Segura et al. 2005). Lately, Rugheimer et al. (2015) have modelled the effect of an M star radiation field on exoplanet atmospheres based on the *Hubble Space Telescope* (*HST*) UV spectra of six exoplanet host stars (France et al. 2013). These stars are apparently only weakly active, as none of them displays Hα emission. Yet their *HST* spectra show hot emission lines proving the presence of a chromosphere and transition region. The lower limit of the chromospheric UV flux and its dependence on stellar parameters has not been constrained so far. Similarly, on the high end of the activity range, with exceptions such as AD Leo (e.g. Sanz-Forcada & Micela 2002; Crespo-Chacón et al. 2006), the frequencies and luminosities of flares on M dwarfs are still largely unknown.

There has been significant recent progress in studies of M dwarf flares based on data from the main *Kepler* mission (Ramsay et al. 2013; Davenport et al. 2014; Hawley et al. 2014; Lurie et al. 2015). The time resolution of 1 min obtained in the *Kepler* short-cadence (SC) data proves essential for catching small events, adding to the completeness of the observed flare distributions and enabling the examination of flare morphology. The drawback is that these results are limited to individual objects or a very small group of bright stars. The K2 mission gives access to much larger samples of bright M dwarfs, for which we can examine the relation between flaring and rotation in a statistical way, albeit at lower cadence. In this work we establish, to our knowledge for the first time, a direct connection between white-light flaring and stellar rotation rate.

As described above, the sample selection is the key to success in constraining the rotation–activity relation of M dwarfs. We present our sample in Section 2. In Section 3, we derive the stellar parameters. This is necessary in order to investigate the dependence of rotation and activity on effective temperature (T_{eff}) and mass (M_*), and to compute commonly used activity indices which consist of normalizing the magnetically induced emission (X-ray, UV, etc.) to the bolometric luminosity. We then describe the analysis of K2 data involving the detection of flares and rotation periods (Section 4), archival X-ray (Section 5) and UV (Section 6) data. We present our results in Section 7. The implications are discussed in Section 8, and we provide a summary in Section 9.

2 SAMPLE

This work is based on all bright and nearby M dwarfs from the Superblink proper motion catalogue by Lépine & Gaidos (2011, henceforth LG11) observed within the K2 mission's campaigns C0–C4. The Superblink catalogue comprises an All-Sky list of 8889 M dwarfs (SpT K7–M7) brighter than $J = 10$, within a few tens of parsec. Many other programmes focusing on M stars are carried out within the K2 mission, and rotation periods have been measured for more than a thousand M stars during the main *Kepler* mission (McQuillan et al. 2013). However, a careful sample selection comprising stars with already known or easily accessible magnetic activity characteristics is mandatory to nail down the rotation–activity relation. The majority of the *Kepler* stars are too distant (>200 pc) and, therefore, too faint for the *ROSAT* All-Sky Survey, the main source for X-ray studies of widely dispersed samples. The proper-motion-selected M stars of the LG11 catalogue are much closer and consequently brighter, facilitating the detection of both rotation periods and X-ray and UV emission.

A total of 134 Superblink M dwarfs have been observed in K2 campaigns C0–C4. Henceforth, we will refer to these objects as the 'K2 Superblink M star sample'. The target list is given in Table 1. We list the identifier from the EPIC catalogue, the campaign in which the object was observed, the designation from the *Third Catalog of Nearby Stars* (CNS 3; Gliese & Jahreiß 1991), magnitudes in the *Kepler* band and further parameters, the calculation of which is described in the next section.

3 FUNDAMENTAL STELLAR PARAMETERS

We derive physical parameters of the K2 Superblink M stars (effective temperature, mass, radius, and bolometric luminosity) by adopting empirical and semi-empirical calibrations from Mann et al. (2015), which are based on the colour indices $V-J$ and $J-H$, and on the absolute magnitude in the 2 MASS K band, M_{K_S}. The calibrations of Mann et al. (2015) are valid for dwarf stars, and can be expected to hold for the K2 Superblink M star sample which has been cleaned by LG 11 from contaminating giants. Due to a press error some wrong values appeared in the tables of Mann et al. (2015). We use here the correct values reported in the erratum (Mann et al. 2016). Stellar magnitudes and their uncertainties are obtained from the UCAC4 catalogue (Zacharias et al. 2013) which provides 2MASS near-IR photometry and V-band magnitudes from *The AAVSO Photometric All Sky Survey* (*APASS*; Henden & Munari 2014). These latter ones are more accurate and have significantly better precision than the V-band magnitudes given in LG 11. For the six stars with no V magnitude in UCAC4, we found measurements in Data Release 9 of the APASS catalogue.[1]

[1] https://www.aavso.org/apass (Henden et al. 2016)

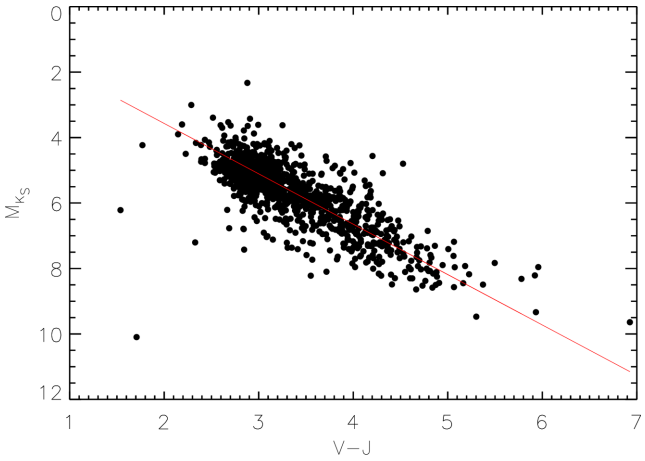

Figure 1. Calibration of the linear relation between absolute K_S magnitude, M_{K_S}, and $V - J$ colour obtained from a sample of 1078 M dwarfs with measured trigonometric parallax in LG11 (black circles). Our best-fitting model is represented by a red solid line. The residuals have a scatter of 0.56 mag.

We derive an empirical linear calibration to calculate M_{K_S} for our sample, using a list of 1078 M dwarfs with apparent K_S magnitude from UCAC 4 and trigonometric parallax in LG 11. This allows us to obtain estimates for M_{K_s} independent on the trigonometric parallax which is available for only 27 stars in our sample. The best linear least-squares fit to the data is obtained through a Monte Carlo analysis. This approach provides more realistic errors than simple least-squares fitting because the uncertainties are derived from posterior distributions of the parameters and take into account all the errors affecting the measurements.

Specifically, we generate 10 000 synthetic samples (each composed of 1078 stars) drawing $V - J$ and M_{K_S} randomly from 2D normal distributions with mean equal to the observed values and standard deviation (henceforth STD) equal to the uncertainties. We then fit to each of the 10 000 representations a straight line with the IDL[2] `FITEXY` routine, assuming for each simulated point the original errors in both variables. The best-fitting relation is then defined by the median values and STD of the a posteriori Monte Carlo distribution for the coefficients in the linear fit, given by

$$M_{K_S} = 0.49(\pm 0.02) + 1.539(\pm 0.006) \cdot (V - J). \quad (1)$$

The residuals of this solution, which is applicable in the range $1.54 < V - J < 6.93$, show an rms of 0.56 mag. In Fig. 1, we show this relation overplotted on the observed data.

All other stellar parameters and their uncertainties are calculated in the same manner through a Monte Carlo analysis. In particular, the stellar effective temperatures ($T_{\rm eff}$) are obtained from the calibration relation which uses $V - J$ and $J - H$ (equation 7 in Mann et al. 2015), while radii (R_*) and masses (M_*) are calculated from relations with M_{K_S} (equations 4 and 10 in Mann et al. 2015, respectively), and the bolometric correction BC_K is derived through a third-degree polynomial with $V - J$ as independent variable (presented in table 3 of Mann et al. 2015).

Thus, we first generate for each star a sample of 10 000 synthetic $V - J$, $J - H$, and M_{K_S} data sets drawn from normal distributions with mean and sigma equal to the observed value and its error. Then we apply to each star the above-mentioned calibrations from Mann et al. (2015). The best estimate of each parameter ($T_{\rm eff}$, R_*, M_* and BC_K) is then obtained as the median value of the corresponding a posteriori distribution, with its STD assumed as the uncertainty.

To provide conservative estimates of the stellar parameters, the uncertainties representing the scatter of the relations of Mann et al. (2015, see Tables 1–3 therein) are propagated into the Monte Carlo process. Specifically, for $T_{\rm eff}$ we consider the scatter in the difference between the predicted and the spectroscopically observed temperature (48 K), and the typical uncertainty on the spectroscopic value of $T_{\rm eff}$ (60 K) adding both in quadrature, while for BC_K we consider the uncertainty of 0.036 mag. These additional uncertainties are taken into account in the Monte Carlo analysis when drawing randomly the samples. For radius and mass, Mann et al. (2015) provide relative uncertainties of 2.89 and 1.8 per cent, respectively. These values are calculated from the median values of our posterior distributions for R_* and M_* and are then added in quadrature to their STD.

Mann et al. (2015) argue that some of the above-mentioned relations for the stellar parameters can be improved by including an additional term involving metallicity ([Fe/H]). We found [Fe/H] measurements in the literature (Newton et al. 2014) for only six stars from the K2 Superblink M star sample, and we verified for these objects that the radii and temperatures derived by taking account of [Fe/H] (equations 5 and 6 in Mann et al. 2015) are compatible with our estimates described above.

From BC_K and M_{K_S} we calculate the absolute bolometric magnitudes of our sample, which are then converted into luminosities assuming the absolute bolometric magnitude of the Sun is $M_{\rm bol,\odot} = 4.7554$. We note, that the distances we infer from our M_{K_s} values and the observed K_s magnitudes are systematically larger, on average by about ∼25 per cent, than the photometric distances presented by LG11 for the same stars. For the 27 stars with trigonometric parallax in the literature (LG11; Dittmann et al. 2014) our newly derived photometric distances are in excellent agreement with the trigonometric distances. In the near future, *Gaia* measurements will provide the ultimate and accurate distances for all K2 Superblink M stars. In the meantime, as corroborated by the comparison to trigonometric parallaxes, our estimates, which are based on the most accurate photometry available to date, can be considered as a fairly reliable guess on the distances.

All stars in the K2 Superblink M star sample have a photometric estimate of the SpT in LG 11, based on an empirical relation of SpT with $V - J$ colour which was calibrated with SDSS spectra. Since we use here the higher precision UCAC 4 V-band magnitudes, for consistency with our calculation of the other stellar parameters, we derive an analogous relation between $V - J$ and SpT. To this end, we make use of 1173 stars classified as K7 or M-type dwarfs by Lépine et al. (2013) based on spectroscopy. We group the stars in bins of 0.5 spectral subclasses, with K7 corresponding to −1, M0 to 0, and so on until M4.5, which is the last sub-type for which we have enough stars in the calibration sample for a useful fit. We calculate the mean and STD of $V - J$ for each SpT bin, and notice that the data can be fitted with a combination of two straight lines for the ranges [K7,M2] and [M2,M4.5] (see Fig. 2). Our fit, performed through a Monte Carlo procedure as described above, results in the relations

$$V - J = 2.822(\pm 0.067) + 0.285(\pm 0.061) \cdot SpT \quad (2)$$

$$V - J = 2.53(\pm 0.29) + 0.432(\pm 0.093) \cdot SpT \quad (3)$$

[2] IDL is a product of the Exelis Visual Information Solutions, Inc.

Table 2. Rotation and activity parameters derived from the K2 light curves. The full table is available in the electronic version of the journal.

EPIC ID	P_{rot} (d)	Method	Flag	R_0	R_{per} (per cent)	S_{ph} (ppm)
202059188	0.69	LS	*Y*	0.01	2.754	10 520.9
202059192	35.22	SINE	*Y*	0.78	0.559	1844.1
202059193	19.01	LS	?	0.42	0.469	1161.4
202059195	42.46	SINE	*Y*	0.63	1.814	6447.7
202059198	27.31	LS	*Y*	0.61	0.883	2802.3
202059199	–	–	*N*	–	0.877	2508.0
202059203	–	–	*N*	–	0.273	635.6
202059204	7.89	ACF	*Y*	0.18	2.760	8494.3

Table 3. X-ray parameters derived from archival data. For stars with multiple detections the mean X-ray luminosity is given. $Sep_{x,opt}$ are the separations between X-ray and K2-EPIC position.

EPIC ID	$\log L_x$ (erg s^{-1})	$Sep_{x,\,opt}$ (arcsec)	Ref.cat
202059204	28.6 ± 0.2	6.2, 6.2	BSC, BSC
202059229	29.2 ± 0.2	2.9, 2.9	BSC, BSC
202059231	28.2 ± 0.3	13.3, 13.3	FSC, FSC
201482319	28.2 ± 0.2	7.6, 14.0	BSC, 2RXP
201518346	26.8 ± 0.2	7.2, 10.8	2RXP, BSC
201675315	27.1 ± 0.2	1.4, 1.4	3*XMM*, 3*XMM*
201806997	29.4 ± 0.2	6.8, 6.8	BSC, BSC
201917390	28.5 ± 0.2	8.4, 29.1	BSC, XMMSL
201842163	28.5 ± 0.2	22.8, 22.8	BSC, BSC
201909533	28.8 ± 0.2	2.8, 2.8	BSC, BSC
202571062	29.5 ± 0.2	13.0, 5.6	$XMMSL_1$, $XMMSL_2$
204927969	28.1 ± 0.2	2.3, 2.3	BSC, BSC
204957517	27.8 ± 0.2	1.0, 1.0	2RXP, 2RXP
205467732	27.4 ± 0.3	8.9, 8.9	FSC, FSC
205913009	26.1 ± 0.2	0.6, 0.6	3*XMM*, 3*XMM*
206019392	26.2 ± 0.2	0.3, 9.0	3*XMM*, 2RXP
206208968	28.8 ± 0.2	18.3, 18.3	BSC, BSC
206262336	28.5 ± 0.2	13.4, 13.4	BSC, BSC
206349327	28.7 ± 0.3	2.2, 2.2	BSC, BSC
210434976	28.4 ± 0.2	26.3, 26.3	BSC, BSC
210500368	27.9 ± 0.3	0.8, 0.8	3*XMM*, 3*XMM*
210613397	29.4 ± 0.2	11.0, 11.0	BSC, BSC
210651981	28.7 ± 0.2	8.2, 12.5	XMMSL, BSC
210707811	28.3 ± 0.3	18.3, 18.3	FSC, FSC
210741091	28.7 ± 0.2	6.0, 10.7	$2RXP_2$, $2RXP_1$
211111803	28.7 ± 0.3	17.8, 17.8	FSC, FSC

which are valid for $2.5 \leq V - J \leq 3.4$ and $3.4 \leq V - J \leq 4.5$, for the hotter (equation 2) and cooler (equation 3) SpT, respectively. We use this calibration to classify the K2 Superblink M star sample, by rounding the results of the linear relations to the closest spectral subtype. Nine K2 Superblink M stars have $V - J$ colours slightly beyond the boundaries for which we calibrated equations (2) and (3) and we extrapolate the relations at the ends to SpT K5 and M5, respectively. No star deviates by more than 0.5 spectral subclasses from equations (2) and (3). The spectroscopically determined SpT from the literature, which are available for roughly three dozens of the K2 Superblink M stars, are in excellent agreement with our values (see Reid et al. 2004; Reiners et al. 2012; Lépine et al. 2013).

In Table 1, we provide the photometry (*Kepler* magnitude K_p, V, J, and K_s), the distances obtained from the absolute K-band magnitude, the fundamental parameters (M_*, R_*, $\log L_{bol}$ and T_{eff}) and the SpT derived as described above. The few stars with M_{K_s} slightly more than 3σ smaller than the lower boundary of the calibrated range ($4.6 < M_{K_s} < 9.8$) are flagged with an asterisk in Table 1.

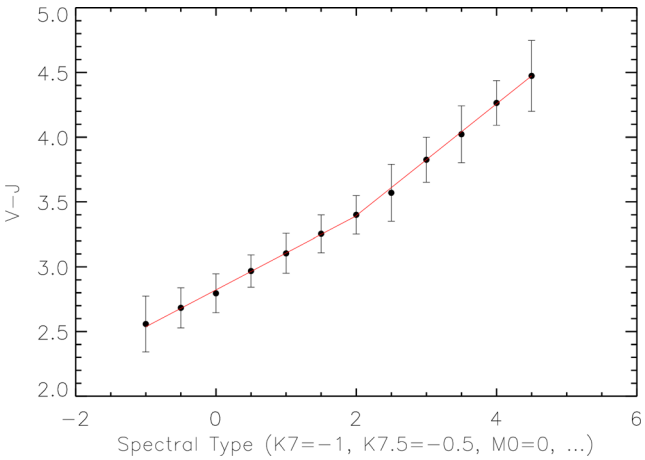

Figure 2. Calibration of the relation between SpT and $V - J$ obtained from a sample of 1173 M dwarfs with spectroscopically determined SpT in Lépine et al. (2013). We fit the data with two straight lines (red solid lines), one for stars with subtypes earlier than M2 and the other one for those with subtypes later than M2.

Stars for which the K2 photometry – and in some cases also the optical/IR photometry used by us to calculate the stellar parameters – comprises a potential contribution from a close binary companion are discussed in detail in the Appendix B. These stars are also highlighted in Table 1 and flagged in all figures where relevant. The Gl 852 AB binary is represented in our target list by two objects (EPIC 206262223 and EPIC 206262336) but they are not resolved in the K2 aperture,[3] i.e. only the combined light curve of both stars is at our disposition. We compute the stellar parameters for both components in the binary using the individual V magnitudes from Reid et al. (2004); then we assign the rotational parameters and the X-ray/UV emission to the brighter, more massive star (EPIC 206262336) and we do not consider the secondary (EPIC 206262223) any further.

[3] Our analysis relies on the data reduction performed by A.Vanderburg; see Section 4.

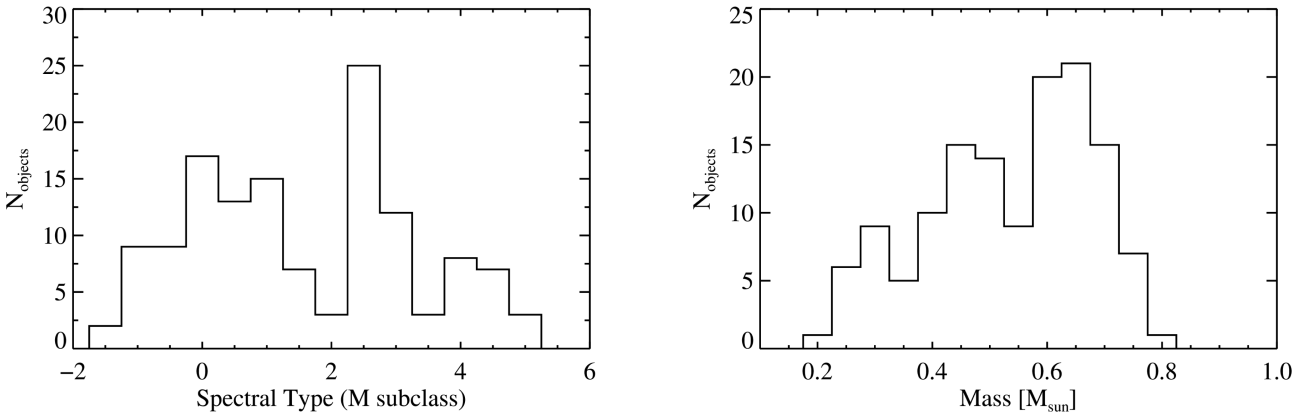

Figure 3. Distribution of SpT and masses for the K2 Superblink M star sample observed in campaigns C0–C4. Negative indices denote SpT earlier than M, where the value −1 stands for K7. See the text in Section 3 for details.

The distributions of SpT and mass for the K2 Superblink M star sample are shown in Fig. 3. Covering SpT K5–M5 (masses between about 0.2 and 0.9 $M_{\odot}$), this is an excellent data base for investigating the connection between rotation and activity across the fully convective boundary (SpT ∼M3/M4).

4 K2 DATA ANALYSIS

We base our analysis of K2 time series mostly on the light curves made publicly available by A.Vanderburg (see Vanderburg & Johnson 2014, and Section 4.1). We use the 'corrected' fluxes in which the features and trends resulting from the satellite pointing instability have been eliminated. All stars of the K2 Superblink M star sample have been observed in long-cadence (LC) mode with time resolution of $\Delta t_{\rm LC} = 29.4$ min. Nine stars have in addition SC data available ($\Delta t_{\rm SC} = 1$ min). In the following, where not explicitly stated, we refer to the LC data.

Our analysis comprises both the measurement of rotation periods and an assessment of photometric activity indicators. In particular, the identification of flares is of prime value both for activity studies and for obtaining a 'cleaned' light curve allowing us to perform more accurate diagnostics on the rotation cycle, e.g. its amplitude. The main limitation of the LC data is the difficulty in identifying short-duration flares, as a result of poor temporal resolution combined with the presence of some residual artefacts from instrumental effects in the light curves that have not been removed in the K2 data reduction pipeline. However, in this work we aim at elaborating trends between activity and rotation, and for this purpose completeness of the flare sample is less important than having statistically meaningful numbers of stars.

Rotation and activity diagnostics are determined with an iterative process in which we identify 'outliers' in the K2 light curves. This involves removing any slowly varying signal by subtracting a smoothed light curve from the original data. The appropriate width of the boxcar in the smoothing process depends on the time-scale of the variation to be approximated, i.e. on the length of the rotational cycle. Therefore, we start the analysis with a first-guess period search on the original, corrected light curve. We use three methods to determine rotation periods which are laid out in Section 4.4. Before presenting the details of our period search we describe how we prepare the light curves and how we extract the flares and 'clean' the corrected light curves further, thus removing both astrophysical flare events and residual noise from the data reduction.

4.1 Data preparation

We download the light curves reduced and made publicly available by A. Vanderburg.[4] The data reduction steps are described by Vanderburg & Johnson (2014). In short, the authors extracted raw photometry from K2 images by aperture photometry. The variability in the resulting light curves is dominated by a zigzag-like pattern introduced by the instability of the satellite pointing and its correction with help of spacecraft thruster fires taking place approximately every 6 h. This artificial variability can be removed by a 'self-flat fielding' process described in detail by Vanderburg & Johnson (2014). We base our analysis on these 'corrected' or 'detrended' light curves to which we apply some additional corrections described below.

Upon visual inspection of each individual corrected light curve, we notice some flux jumps. As explained by A.Vanderburg in his data release notes[5] such offsets can arise due to the fact that he divides the light curves in pieces and performs the data reduction separately on each individual section. In stars with long-term variations these offsets are clearly seen to be an artefact of the data reduction, and we remove them by applying a vertical shift to the light curve rightwards of the feature. Note that, since the absolute fluxes are irrelevant for our analysis it does not matter which side is used as the baseline for the normalization. While such flux jumps are evident in light curves with slow variations, for stars with short periods it is much more difficult to identify such systematic offsets and even if they are identified it is impossible to perform the normalization without a priori knowledge of the (periodic) variation pattern. However, since such short-period light curves comprise many rotational cycles, the period search is much less sensitive to such residual artefacts than it is for long-period light curves.

In a second step, we remove all cadences in which the satellite thrusters were on (and the telescope was moving). The thruster fires are shorter than the cadence of observations in LC mode such that each of the corresponding gaps regards a single data point. Several light curves have spikes and decrements produced by incomplete background removal or individual null values among the fluxes. We identify such obvious artefacts by visual inspection of each

[4] The reduced K2 light curves were downloaded from https://www.cfa.harvard.edu/∼avanderb/k2.html.

[5] The technical reports on the detrending process carried out by A.Vanderburg are accessible at https://www.cfa.harvard.edu/∼avanderb/k2.html.

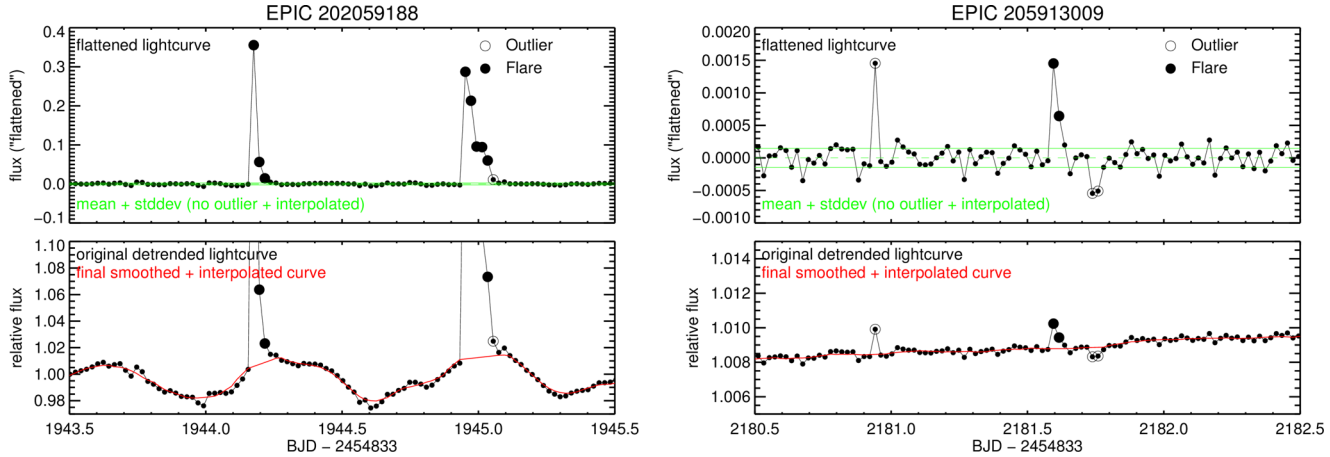

Figure 4. Examples of light curves illustrating the procedure applied to identify flares. Data points identified as flares are indicated, as well as other outlying points, according to the procedure described in Section 4.2.

individual light curve and remove the respective data points. We then fill all gaps in the K2 light curves, i.e. all data points separated by multiples of $\Delta t_{\rm LC}$, by interpolation on the neighbouring data points. Evenly spaced data is required for the autocorrelation function (ACF), one of the methods we use for the period search (see Section 4.4.1). We add Gaussian noise to the interpolated data points. To avoid that the width of the distribution from which the errors are drawn is dominated by the rotational variation we use only the nearest data points to the right and to the left of the gap to define mean and sigma of the Gaussian.

4.2 Identification of flares

Then we start the iterative flare search and cleaning process. Our approach is similar to the methods presented in previous systematic *Kepler* flare studies (Hawley et al. 2014, and subsequent papers of that series). Specifically, our procedure consists in (i) boxcar smoothing of the light curve, (ii) subtraction of the smoothed from the original light curve (i.e. removal of the rotational signal), and (iii) flagging and removal of all data points which deviate by more than a chosen threshold from the subtracted curve. We repeat this procedure three times with successively smaller width of the boxcar. Subsequently, the removed cadences are regenerated by interpolation and addition of white noise as described above. This provides a light curve that is free from flares (henceforth referred to as the 'cleaned' light curve). When subtracted from the original corrected data, the result is a flat light curve (henceforth referred to as the 'flattened' light curve) in which the rotational variation has been removed and the dominating variations are flares, eclipses and artefacts.

A significant fraction of the data points that have been removed in the above σ-clipping process are isolated cadences. Such events are found both as up- and downward excursions in the flattened light curves. The number of upward outliers is for most light curves much larger than the number of downward outliers, suggesting that many of these events are genuine flares. However, we assume here a conservative approach aimed at avoiding counting spurious events as flare. Therefore, we select all groups of at least two consecutive upwards deviating data points as flare candidates. In practice, this means that the minimum duration of the recognized flares is $\sim$1 h (two times the cadence of 29.4 min). Note, that as a result of the sigma-clipping, all flare peaks ($F_{\rm peak}$) have a minimum significance of 3σ, as measured with respect to the mean and STD of the flattened light curve from which outliers have been removed, which is defined and further discussed in Section 4.3. Finally, we require that $F_{\rm peak}$ must be at least twice the flux of the last of the data points defining the flare ($F_{\rm last}$). As shown below, this last criterion removes 'flat-topped' events from our list of bona-fide flares which we trust less than 'fast-decay' events given the possibility of residual artefacts from the data acquisition and reduction.

A zoom into two examples of LC light curves with flares is shown in Fig. 4 and illustrates our flare search algorithm. The lower panel shows the original, detrended light curve and overlaid (in red) the smoothed light curve. The upper panel shows the result from the subtraction of these two curves, i.e. the flattened light curve. We highlight data points identified as outliers (open circles), and data points that belong to bona-fide flares (filled circles). The example on the right demonstrates the inability of recognizing short flares with our detection procedure. SC data from the main *Kepler* mission have shown that many flares on active M stars are, in fact, significantly shorter than 1 h (see e.g. Hawley et al. 2014). SC light curves are available for nine stars from the K2 Superblink M star sample. The analysis of SC light curves will be described elsewhere. In this work, we use the SC data only as a cross-check on the quality of our flare search criteria applied to the LC data (see below and Fig. 5). We recall that we aim at a conservative approach, avoiding at best possible spurious events in the flare sample, because our aim is to study trends with rotation.

To summarize, the parameters of our flare search algorithm are (i) the width of the boxcar (adapted individually according to the first-guess period), (ii) the threshold for outliers identified in the σ-clipping process (adopted to be 3σ), (iii) the minimum number of consecutive data points defining a flare (2), and (iv) the flux ratio between the flare peak bin and the last flare bin ($F_{\rm peak}/F_{\rm last} \geq 2$). The values for these parameters have been chosen by testing various combinations of criteria (i)–(iv) with different parameter values and comparing the results to a by-eye inspection of the 'flattened' light curves. In particular, criterion (iv) is introduced after a comparison of LC and SC light curves which shows that, generally, the LC flare candidates correspond to analogous features in the SC data but in some cases the features are very different from the canonical flare shape (characterized by fast rise and exponential decay). Fig. 5 demonstrates that with criterion (iv) we de-select such broad events from the list of bona-fide flares: two flare candidates according to

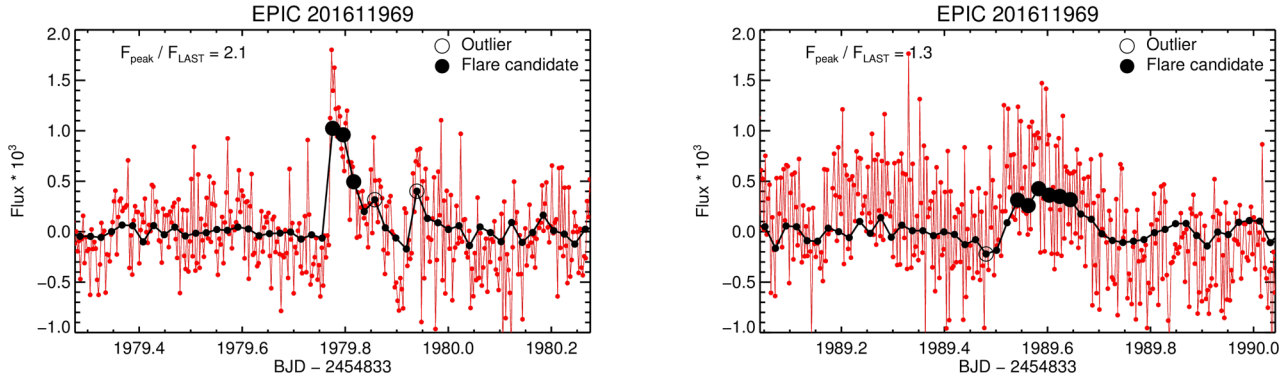

Figure 5. Portion of the LC (black) and SC (red) K2 light curve for EPIC 201611969. Flare candidates in LC data according to criteria (i)–(iii) described in Section 4.2 are marked with large filled circles. On the left a bona-fide flare, on the right a flare candidate which we discard on the basis of its shape ($F_{\rm peak}/F_{\rm last} < 2$). The SC light curve has been binned to a cadence of 4 s; any vertical offset is the result of the different analysis for SC and LC data and is irrelevant for our purpose of comparing the shape of flare candidates.

criterion (i)–(iii) are shown; the event on the left-hand panel is a bona-fide flare according to criterion (iv) while the event on the right does not fulfil $F_{\rm peak}/F_{\rm last} \geq 2$.

4.3 Residual variability and photometric noise

In Fig. 6, we show the STD of the flattened light curves, $S_{\rm flat}$, for two cases: including and excluding the data points identified as outliers. The 'outliers' comprise flares, transits or eclipses, and artefacts from the data reduction. Therefore, for the case without outliers (red circles) the STD is calculated on the residual light curve from which the known astrophysical sources of variability have been removed, and it can be expected to represent the noise level in our data.

In Fig. 6, we compare our STD $S_{\rm flat}$ to the estimated precision of K2 light curves provided for campaigns C0 and C1 in the data release notes of A.Vanderburg (see footnote to Section 4.1). That estimate

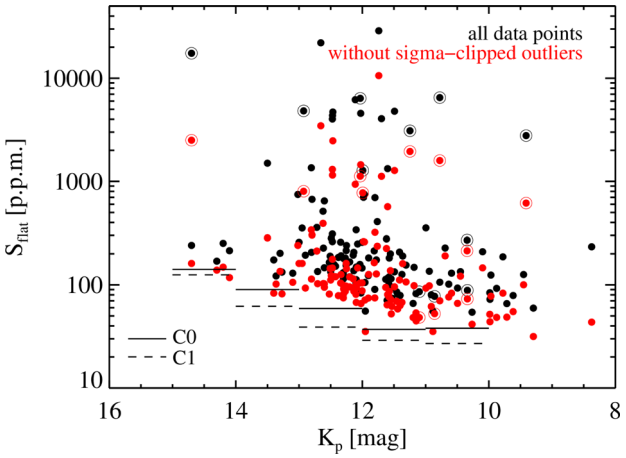

Figure 6. STD for the light curves of the Superblink stars after 'flattening' by removal of the rotational signal as described in Section 4.2. $K_{\rm p}$ is the magnitude in the *Kepler* band. $S_{\rm flat}$ is calculated for two data sets: the full light curve (black circles) and the light curve without all data points that were identified as outliers during the clipping process (red circles). Horizontal lines represent the 6 h-precisions for C0 and C1 calculated by A.Vanderburg (see footnote to Section 4.1) for a sample of cool dwarfs drawn from different K2 Guest Observer programmes. Stars with a possible contribution in the K2 photometry from an unresolved binary companion are highlighted with large annuli.

represents the 6 h-precision based on a sample of cool dwarfs that is not clearly specified. Our $S_{\rm flat}$ measurements suggest a somewhat lower precision for the K2 Superblink M star sample. This might be due to differences in the definitions. Vanderburgs's 6 h-precisions are medians for their sample and the scatter among their stars is much larger than the factor 2 difference with our $S_{\rm flat}$ values. Also, we measure the STD on the full light curve while Vanderburg's precisions are based on a running 6 h mean. An alternative explanation for the apparently different photometric precisions could lie in different activity levels of the two samples, implying residual fluctuations of astrophysical origin in our 'noise'. In fact, in Section 7.5 we present evidence that $S_{\rm flat}$ comprises an astrophysical signal. Overall, our analysis presented in Fig. 6 confirms the high precision achieved in K2 light curves with the detrending method applied by A.Vanderburg.

4.4 Period search

We explore multiple approaches to measure rotation periods on the K2 data.

4.4.1 Period search on detrended light curves

We apply standard time series analysis techniques, the Lomb Scargle (LS) periodogram and the ACF, to the detrended K2 light curves made publicly available (see Vanderburg & Johnson 2014). As mentioned in Section 4, as a first step we perform the period search directly on the corrected version of the downloaded light curves with the purpose of adapting the boxcar width in the course of the search for flares. We then repeat the period search on the 'cleaned' light curves obtained after the σ-clipping process and the regeneration of the missing data points through interpolation, i.e. after removal of the flares and other outliers. The analysis is carried out in the IDL environment using the SCARGLE and A_CORRELATE routines.

Periodograms and ACFs have already been used successfully to determine rotation periods in *Kepler* data (e.g. McQuillan et al. 2013, 2014; Nielsen et al. 2013; Rappaport et al. 2014). As a cross-check on our procedure, we have downloaded *Kepler* light curves from the *Mikulski Archive for Space Telescopes*[6] for some M stars

[6] We downloaded the *Kepler* light curves from the Target Search page at https://archive.stsci.edu/kepler/kepler_fov/search.php.

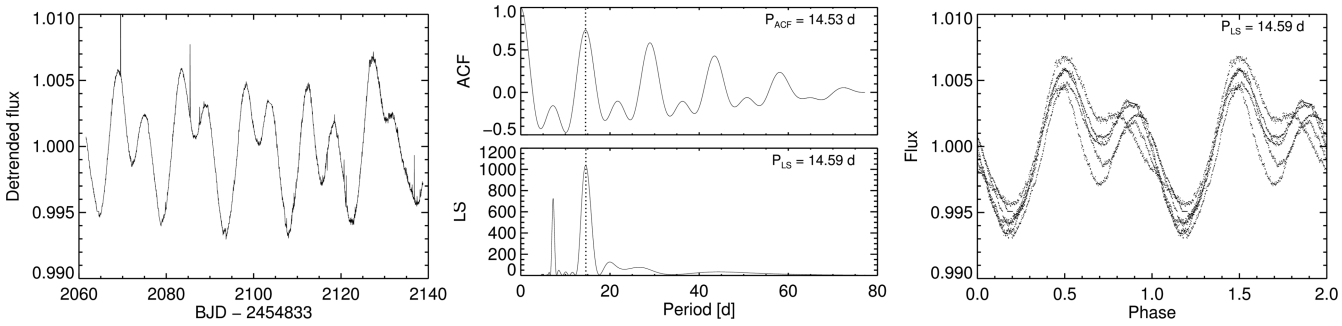

Figure 7. Example of detrended K2 light curve (left-hand panel), ACF and LS periodogram (middle panel), and light curve folded with the ACF period (right-hand panel).

from the McQuillan et al. (2013) sample and we have verified that we correctly reproduce the published periods.

Following McQuillan et al. (2013), in our use of the ACF method we generally identify the rotation period as the time lag, $k \cdot \Delta t_{\rm LC}$ with integer number k, corresponding to the first peak in the ACF. Subsequent peaks are located at multiples of that period, resulting in the typical oscillatory behaviour of the ACF. Exceptions are double-peaked light curves where the ACF presents two sequences of equidistant peaks (see e.g. Fig. 7). Such light curves point to the presence of two dominant spots, and we choose the first peak of the sequence with higher ACF signal as representing the rotation period. McQuillan et al. (2013) have performed simulations that demonstrate the typical pattern of the ACF for different effects in the light curve, such as changing phase and amplitude, double peaks, and linear trends. All these features are also present in the K2 data, although less pronounced than in the much longer main *Kepler* mission time series examined by McQuillan et al. (2013).

The classical periodogram is based on a Fourier decomposition of the light curve. In the form presented by Scargle (1982), it can be applied to unevenly sampled data and is essentially equivalent to least-squares fitting of sine-waves. Realistic time series deviate from a sine-curve, and are subject to the effects described above. This introduces features in the power spectrum. Since the dominating periodicity in the K2 Superblink stars is reasonably given by the stellar rotation cycle, the highest peak of the periodogram can be interpreted as representing the rotation period. The LS periodograms are computed here for a false-alarm probability of 0.01 using the fast-algorithm of Press & Rybicki (1989).

In Fig. 7, we show an example for a detrended K2 light curve, its LS periodogram and ACF, and the light curve folded with the derived period. An atlas with the phase-folded light curves for all periodic stars is provided in Appendix A.

4.4.2 *Period search on un-detrended light curves*

As an independent check we derive the stellar rotation periods with the Systematics-Insensitive periodogram (SIP) algorithm developed by Angus, Foreman-Mackey & Johnson (2016), that produces periodograms calculated from the analysis of the raw K2 photometric time series. For each observing campaign, these are modelled with a linear combination of a set of 150 'eigen light curves' (ELC), or basis functions, that describe the systematic trends present in K2 data, plus a sum of sine and cosine functions over a range of frequencies.[7]

[7] K2 raw and 'eigen' light curves were downloaded from http://bbq.dfm.io/ketu/lightcurves/ and http://bbq.dfm.io/ketu/elcs/.

For each test frequency, the system of linear equations is solved through a least-square fit to the data. The periodogram power is determined as described in Angus et al. (2016), by calculating the squared signal-to-noise ratio $(S/N)^2$ for each frequency. $(S/N)^2$ is a function of the sine and cosine coefficients (i.e. the amplitudes), where the frequencies corresponding to amplitudes not well constrained by the fit are penalized. The stellar rotation period is finally calculated as the inverse of the frequency having the highest power.

4.4.3 *Sine-fitting of stars with long periods*

The techniques described in Sections 4.4.1 and 4.4.2 are limited to periods shorter than the duration of the K2 campaigns (33 d for C0 and 70–80 d for the other campaigns). However, by visual inspection of the light curves, we identify 11 stars with clearly sine-like variations that exceed the K2 monitoring time baseline. For these objects, a least-squares fit allows us to constrain the rotation periods. The fitting was done with the routine CURVE_FIT in the PYTHON package SCIPY (Jones et al. 2001). As initial guesses for the parameters we used four times the STD as amplitude, a period of 30 d, and a phase of 0.0, but the results do not depend on this choice. For all 11 light curves the routine converges on a unique solution independent of the choice of the initial guesses for the parameters. In three cases, the sinecurve provides only a crude approximation because the light curve is not symmetric around maximum or minimum and shows signs of spot evolution; in these cases the results are treated with caution.

4.4.4 *Comparison of results from different period search algorithms*

The results of the different period search methods are compared in Fig. 8. Generally, the LS and the ACF periods are in excellent agreement.

For further use, based on the agreement between the periods obtained with the two techniques and considering the appearance of the phase folded light curve, we adopt either the ACF or the LS period as rotation period. This selection is made independently by two members of the team (BS and AS), and the results deviate for only few stars. For those dubious cases we make use of the SIP results as cross-check, and we adopt the period (either LS or ACF) which is in better agreement with the SIP 'S/N' period. In addition, for the 11 stars that have their highest peak in the ACF and LS at a period corresponding to the length of the data set ($T_{\rm tot}$) but for which visual inspection reveals a clear (sine-like) pattern indicating a spot-modulation with $P_{\rm rot} > T_{\rm tot}$ we use the periods from the sine-fitting. From a comparison of the values obtained with the ACF

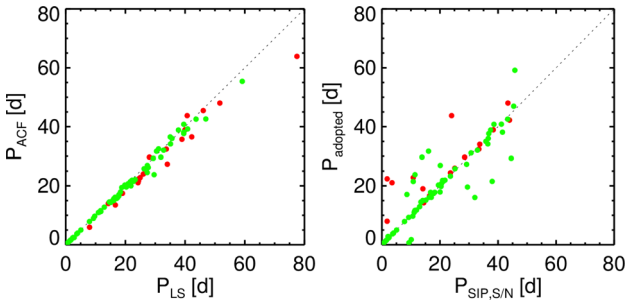

Figure 8. Comparison of the periods derived with the different methods described in Section 4.4. Reliable periods (green; flag 'y' in Table 2), questionable periods (red; flag '?'). Periods equal to or longer than the data set according to the LS and ACF analysis have been determined through sine-fitting and are not shown here.

and with the LS periodogram, we estimate the typical error on our periods to be $\lesssim$3 per cent. The final, adopted periods are given in Table 2 together with a quality flag and reference to the method with which it was derived. Flag '*Y*' stands for reliable periods, '?' for questionable period detections, and '*N*' for no period. These periods are obtained from the 'cleaned' light curves, but due to the robustness of the detection techniques they are in agreement (within <5 per cent) with the periods found on the original, detrended light curves.

5 X-RAY EMISSION

We perform a systematic archive search for X-ray observations of the K2 Superblink M stars. Specifically, we consult the *XMM–Newton* Serendipitous Source Catalogue (3XMM-DR5; Rosen et al. 2016), the *XMM–Newton* Slew Survey Source Catalogue (XMMSL1_Delta6; Saxton et al. 2008), the Second *ROSAT* Source Catalog of Pointed Observations (2RXP) and the *ROSAT* Bright and Faint Source catalogues (BSC and FSC). Our procedure for cross-matching the K2 targets with these catalogues and for deriving X-ray fluxes and luminosities follow those described by Stelzer et al. (2013). That work presented the X-ray and UV emission of the M dwarfs within 10 pc of the Sun. Although that sample was drawn from the same catalogue (LG11), there are only two stars in common with our K2 study because most of the stars that fall in the K2 fields have distances in the range 20–60 pc. We briefly summarize the individual analysis steps here and we refer to Stelzer et al. (2013) for details.

First, in order to ensure that no matches are missed due to the high proper motion of the most nearby stars (stars at <10 pc have proper motions of $\sim$1 arcsec yr^{-1}), the cross-correlation between the K2 target list and the X-ray catalogues is done after correcting the object coordinates from the K2 catalogue[8] to the date of the X-ray observation using the proper motions given by LG11. We then use the following match radii between the X-ray catalogue positions and the K2 coordinates: 40 arcsec for RASS (Neuhäuser et al. 1995), 30 arcsec for XMMSL (Saxton et al. 2008), 25 arcsec for 2RXP (Pfeffermann, Briel & Freyberg 2003) and 10 arcsec for 3XMM-DR5. With one exception all counterparts have much smaller separations than the respective cross-correlation radius (see Table 3). The only doubtful X-ray counterpart is the XMMSL source associated with EPIC 201917390. It has a separation close to the edge of our match circle which – as stated by Saxton et al. (2008) – is a generous interpretation of the astrometric uncertainty of the XMMSL. Since the same star is also clearly identified with a RASS source at an X-ray luminosity within a factor of 2 of the XMMSL source, we decide to keep the XMMSL counterpart. For all but one of the X-ray detected stars the rotation period could be determined. The exception is EPIC 210500368 for which hints for pseudo-periodic variations in the K2 light curve can be seen by-eye but the ACF and LS periodograms show no dominant peak.

After the identification of the X-ray counterparts, we compute their 0.2–2 keV flux assuming a 0.3 keV thermal emission subject to an absorbing column of $N_{\rm H} = 10^{19}$ cm^{-2}. The *ROSAT* count-to-flux conversion factor is determined with PIMMS[9] to be $CF_{\rm ROSAT}$ = 2.03 $\times 10^{11}$ cts erg^{-1} cm^{-2} (see also Stelzer et al. 2013) and we apply it to the count rates given in the 2RXP catalogue, the BSC and the FSC. For 3XMM-DR5 sources, we use the tabulated EPIC/pn count rates in bands 1–3 which represent energies of 0.2–0.5, 0.5–1.0, and 1.0–2.0 keV, respectively. We sum the count rates in these bands, and perform the flux conversion for the combined 0.2–2.0 keV band. All 3XMM-DR5 counterparts to K2 Superblink M stars were observed with the EPIC/pn medium filter, and for the $N_{\rm H}$ and kT given above we find in PIMMS a count-to-flux conversion factor of $CF_{\rm 3XMM\text{-}DR5} = 9.22 \times 10^{11}$ cts erg^{-1} cm^{-2}. The XMMSL1 catalogue has the three energy bands already combined in columns 'B5'.

A total of 26 K2 Superblink stars have an X-ray counterpart in the archival data bases that we have consulted. The X-ray fluxes obtained as described above are converted to luminosities using the updated photometric distances of the stars (see Section 3). The X-ray luminosities are given in Table 3 together with the separation between X-ray and optical position and the respective X-ray catalogue. For stars with more than one epoch of X-ray detection, the luminosities are in agreement within a factor of 2 and we provide the mean of the two values. The errors of $L_{\rm x}$ comprise the uncertainties of the count rates and an assumed 20 per cent error of the distances which yield roughly comparable contributions to the error budget. Our assumption on the distance error is motivated by the distance spread between photometric and trigonometric distances for the subsample with both measurements (described in Section 3).

6 ULTRAVIOLET EMISSION

To assess the UV activity of the K2 Superblink stars, we cross-match our target list with the *GALEX-DR5 sources from AIS and MIS* (Bianchi et al. 2011). *GALEX* performed imaging in two UV bands, far-UV (henceforth FUV; $\lambda_{\rm eff}$ = 1528 Å, $\Delta\lambda$ = 1344–1786 Å) and near-UV (henceforth NUV; $\lambda_{\rm eff}$ = 2271 Å, $\Delta\lambda$ = 1771–2831 Å). The All-Sky Survey (AIS) covered $\sim$85 per cent of the high Galactic latitude ($\|b\| > 20^\circ$) sky to $m_{\rm AB} \sim 21$ mag, and the Medium Imaging Survey (MIS) reached $m_{\rm AB} \sim 23$ mag on 1000 deg^2 (e.g. Bianchi 2009).

Analogous to our analysis of the X-ray data, we correct the coordinates from the K2 catalogue to the date of the respective UV observation. We use a match radius of 10 arcsec, but none of the UV counterparts we identify is further than 3 arcsec from the proper

[8] Note, that the coordinates provided in the target lists of the individual K2 campaigns at http://keplerscience.arc.nasa.gov/k2-approved-programs.html refer to epoch 2000, except for campaign C0 where the coordinates seem to refer to the date of observation (2014 Mar–May).

[9] The Portable Interactive Multi-Mission Simulator is accessible at http://cxc.harvard.edu/toolkit/pimms.jsp.

motion corrected K2 position. The *GALEX*-DR5 catalogue provides NUV and FUV magnitudes which we convert to flux densities using the zero-points given by Morrissey et al. (2005).

We isolate the chromospheric contribution to the UV emission from the photospheric part with help of synthetic DUSTY spectra of Allard et al. (2001), following the procedure described by Stelzer et al. (2013). We adopt the model spectra with solar metallicity and $\log g = 4.5$, and we choose for each star that model from the grid which has $T_{\rm eff}$ closest to the observationally determined value derived in Section 3. We then obtain the predicted photospheric UV flux density $[(f_{\rm UV_i,ph})_\lambda]$ in the two *GALEX* bands ($i = NUV$, FUV) from the UV and J-band flux densities of the DUSTY model (i.e. the synthetic $UV_i - J$ colour) and the observed J-band flux density. The model flux densities in the FUV, NUV and J bands are determined by convolving the synthetic spectrum with the respective normalized filter transmission curve. Finally, the FUV and NUV fluxes are obtained by multiplying $(f_{\rm UV_i,ph})_\lambda$ with the effective band width of the respective *GALEX* filter ($\delta\lambda_{\rm FUV} = 268$ Å; $\delta\lambda_{\rm NUV} = 732$ Å); Morrissey et al. (2007). The expected photospheric fluxes ($f_{\rm UV_i,ph}$) are then subtracted from the observed ones to yield the chromospheric fluxes. We refer to these values as 'UV excess', $f_{\rm UV_i,exc}$. Finally, we define the UV activity index as $R'_{\rm UV_i} = \frac{f_{\rm UV_i,exc}}{f_{\rm bol}}$ where $f_{\rm bol}$ is the bolometric flux. The superscript ($'$) indicates, in the same manner as for the well-known Ca II H&K index, that the flux ratio has been corrected for the photospheric contribution.

We find NUV detections for 41 stars from the K2 Superblink M star sample, i.e. roughly 30 per cent, while only 11 stars (∼8 per cent) are identified as FUV sources. Stelzer et al. (2013) have shown that the photospheric contribution to the FUV emission of M stars is negligible while the fraction of the NUV emission emitted by the photosphere can be significant. We confirm here for the K2 Superblink M stars with FUV detections that this emission is entirely emitted from the chromosphere, i.e. $f_{\rm FUV,\,ph}$ is orders of magnitude smaller than the observed FUV flux. The NUV emission of the K2 Superblink M stars is also only weakly affected by photospheric contributions with $f_{\rm NUV,\,ph}$ less than ∼10 per cent of the observed flux for all stars. In Table 4, we provide the observed FUV and NUV magnitudes and the calculated chromospheric excess, $L_{\rm UV_i,exc}$, of all detected objects. The uncertainties for the UV luminosities comprise the magnitude errors and an assumed 20 per cent error on the distances (as in Section 5).

Table 4. UV parameters derived from archival *GALEX* data. Errors on the UV luminosities comprise also an assumed uncertainty of 20 per cent on the distance.

EPIC ID	NUV (mag)	FUV (mag)	$\log L^a_{\rm NUV}$ (erg s^{-1})	$\log L^a_{\rm FUV}$ (erg s^{-1})
201237257	19.95 ± 0.13		28.3 ± 0.2	
201460770	21.89 ± 0.40		27.8 ± 0.3	
201482319	20.17 ± 0.16	21.54 ± 0.48	27.6 ± 0.2	26.9 ± 0.3
201506253	21.20 ± 0.19		28.1 ± 0.2	
201518346	21.16 ± 0.36		26.0 ± 0.2	
201568682	21.07 ± 0.22		28.4 ± 0.2	
201611969	21.85 ± 0.30		27.4 ± 0.2	
201675315	20.95 ± 0.27		28.1 ± 0.2	
201719818	19.14 ± 0.08	22.05 ± 0.47	28.5 ± 0.2	27.3 ± 0.3
201917390	20.20 ± 0.15	21.47 ± 0.38	27.9 ± 0.2	27.3 ± 0.2
201367065	21.41 ± 0.22		28.2 ± 0.2	
201497866	21.28 ± 0.34		27.9 ± 0.2	
201842163	20.02 ± 0.11	21.39 ± 0.29	28.2 ± 0.2	27.6 ± 0.2
201909533	18.45 ± 0.04	20.06 ± 0.12	28.6 ± 0.2	27.9 ± 0.2
204963027	19.86 ± 0.17		28.3 ± 0.2	
204927969	20.18 ± 0.20		27.8 ± 0.2	
204994054	20.70 ± 0.28		28.2 ± 0.2	
206007536	19.99 ± 0.09		28.7 ± 0.2	
206019392	20.07 ± 0.09	22.63 ± 0.42	26.4 ± 0.2	25.3 ± 0.2
206054454	21.44 ± 0.25	22.12 ± 0.46	27.7 ± 0.2	27.4 ± 0.3
206055065	19.87 ± 0.10		29.0 ± 0.2	
206056832	21.45 ± 0.25		28.5 ± 0.2	
206107346	19.02 ± 0.05	21.86 ± 0.30	28.2 ± 0.2	27.0 ± 0.2
206208968	18.89 ± 0.08	20.14 ± 0.21	28.2 ± 0.2	27.6 ± 0.2
206368165	22.54 ± 0.47		27.5 ± 0.3	
206479389	21.57 ± 0.33		27.9 ± 0.2	
206490189	21.96 ± 0.30		27.3 ± 0.2	
210393283	21.57 ± 0.41		28.0 ± 0.3	
210434976	20.18 ± 0.16		27.7 ± 0.2	
210460280	20.76 ± 0.20		27.9 ± 0.2	
210500368	21.80 ± 0.40		27.9 ± 0.3	
210502828	20.49 ± 0.18		28.5 ± 0.2	
210535241	21.75 ± 0.35		28.1 ± 0.2	
210579749	19.58 ± 0.09	21.40 ± 0.40	27.9 ± 0.2	27.1 ± 0.2
210585703	21.97 ± 0.40		27.7 ± 0.3	
210592074	20.33 ± 0.33		28.8 ± 0.2	
210613397	19.69 ± 0.09	21.66 ± 0.39	28.8 ± 0.2	27.9 ± 0.2
210757663	21.65 ± 0.39		28.1 ± 0.3	
210778181	20.30 ± 0.18		28.5 ± 0.2	
211008819	18.81 ± 0.08		28.5 ± 0.2	
211036776	21.08 ± 0.22		27.9 ± 0.2	

[a]Chromospheric excess luminosities after subtraction of the photospheric contribution.

7 RESULTS

7.1 Period statistics and comparison with the literature

We could determine reliable periods for 75 stars (flag 'Y' in Table 2), and periods with lower confidence are found for 22 stars (flag '?'). 12 stars of our sample have a previously reported period based on the same K2 data in Armstrong et al. (2015). In all but two cases those periods agree within 1–2 per cent with our values. The exceptions are EPIC-202059204 for which the light curves used by us (and produced by A.Vanderburg) show no evidence for the 5.04 d period provided by Armstrong et al. (2015), and EPIC-201237257 for which our adopted period is twice the value of 16.2 d presented by Armstrong et al. (2015) based on the maximum peak in both our ACF and LS periodogram. Periods for a small number of K2 Superblink stars have been presented previously also in the following studies: survey in the Southern hemisphere using the All-Sky Automated Survey (ASAS; Kiraga 2012, six stars), HATnet survey in the Pleiades (Hartman et al. 2010, two stars), SuperWASP survey in the Hyades and Pleiades (Delorme et al. 2011, one star), and from the compilation of Pizzolato et al. (2003, one star). They are all in excellent agreement with our values derived from the K2 light curves. For the two stars we have in common with the HATNet survey of field stars presented by Hartman et al. (2011), however, we find strongly discrepant values for the periods: 16.1 d versus 39.0 d in Hartman et al. (2011) for EPIC-211107998 and 12.9 d versus 0.86 d in Hartman et al. (2011) for EPIC-211111803. We see no evidence in the K2 data for the period values determined by Hartman et al. (2011).

All in all, a 73 per cent of the K2 Superblink sample shows periodic variability on time-scales up to ∼100 d. Our period distribution is shown in Fig. 9. Studies of rotation of M stars in the main *Kepler* mission have come up with 63 per cent (McQuillan et al. 2013) and 81 per cent (McQuillan et al. 2014) of stars with detected periods. These differences may reflect the different data sets (each

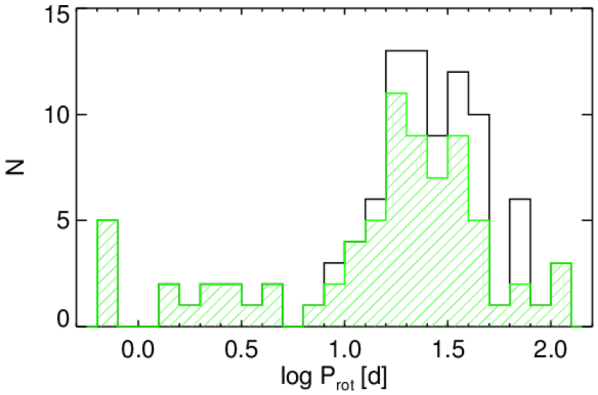

Figure 9. Distribution of the 97 rotation periods determined for the K2 Superblink M star sample. The black histogram represents the full sample of periods, and the overlaid green histogram the subsample of reliable periods (flag 'Y').

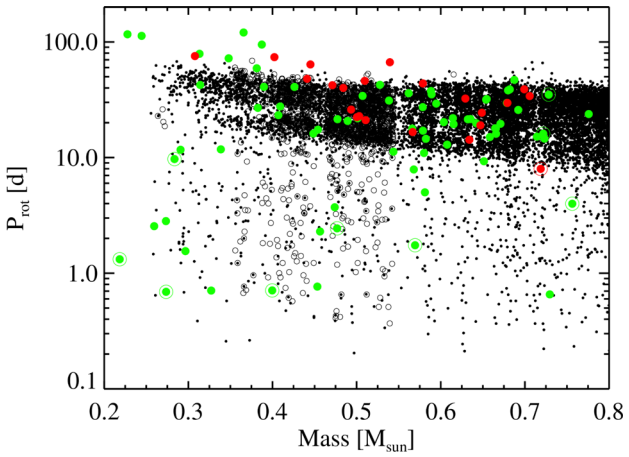

Figure 10. Period versus mass for the K2 Superblink M star sample (green and red symbols for periods flagged 'Y' and '?', respectively). Binaries are marked with annuli (see Appendix B). Data from *Kepler* studies are plotted as open circles (McQuillan et al. 2013) and black dots (McQuillan et al. 2014).

K2 campaign provides a light curve corresponding to the length of about one quarter of *Kepler* data) and detection methods (we use sine-fitting in addition to ACF and periodograms). In particular, we establish here in a relatively unbiased sample of M dwarfs periods of ∼100 d and longer, in agreement with results from ground-based studies (Irwin et al. 2011; Newton et al. 2016). The period distribution of the *Kepler* sample from McQuillan et al. (2013) shows a cut at ∼65 d and McQuillan et al. (2014) explicitly limit their sample to periods <70 d. Note, that McQuillan et al. (2013) have performed the period search on individual *Kepler* Quarters which are of similar duration as the K2 campaigns. In fact, we are able to detect such long periods only thanks to the least-squares sine-fitting. We find that ∼10 per cent of the periods are longer than 70 d. These would not have been detected by the methods of McQuillan et al. (2013, 2014). An additional possible explanation for the absence of long-period variables in McQuillan et al. (2013) – related to photometric sensitivity – is presented in Section 7.3.

7.2 Rotation period and stellar mass

We present the newly derived rotation periods for the K2 Superblink M star sample in Fig. 10 as a function of stellar mass together with results for studies from the main *Kepler* mission. The sample of McQuillan et al. (2013, black open circles) covered stars in the mass range of 0.3–0.55 $M_\odot$ selected based on the $T_{\rm eff}$ and *logg* values from the *Kepler* input catalogue (Brown et al. 2011). Subsequently, McQuillan et al. (2014, black dots) extended this study with similar selection criteria to all stars with $T_{\rm eff} < 6500$ K. Among the most notable findings of these *Kepler* studies was a bimodal period distribution for the lowest masses, and an increasing upper envelope of the period distribution for decreasing mass. While we have too few objects to identify the bimodality, we confirm the upwards trend in the longest periods detected towards stars with lower mass. We are able to measure longer periods than McQuillan et al. (2013, 2014) because we add sine-fitting to the ACF and periodgram period search methods; see Section 7.3 for a more detailed comparison of the period detection techniques and their implications. The fact that we measure periods in excess of ∼100 d only in stars with very low mass ($M \leq 0.45\,M_\odot$) is interesting. If it is a real feature in the rotational distribution, it suggests a change of the spin-down efficiency at the low-mass end of the stellar sequence. Note, however, that the stellar masses at which the upturn is seen to set in does not correspond to the fully convective transition (∼0.35 $M_\odot$) where one might expect some kind of 'mode change' in the dynamo. Also, we cannot exclude that there are detection biases, e.g. the size and distribution of star-spots and their lifetimes could be mass-dependent such that smaller and more quickly changing amplitudes are induced in higher mass stars which would prevent us from detecting very long periods in them. A more detailed investigation of these features must be deferred to studies on a larger sample.

7.3 Activity diagnostics from K2 rotation cycles

We examine now various other diagnostics for rotation and activity derived from the K2 data. These are listed together with the rotation periods in Table 2.

The Rossby number (in column 5) is defined as $R_0 = P_{\rm rot}/\tau_{\rm conv}$, where $\tau_{\rm conv}$ is the convective turnover time obtained from $T_{\rm eff}$ using equation 36 of Cranmer & Saar (2011) and its extrapolation to $T_{\rm eff} < 3300$ K. There is no consensus on the appropriate convective turnover times for M dwarfs beyond the fully convective boundary. As pointed out by Cranmer & Saar (2011), the extrapolated values for late-M dwarfs ($\tau_{\rm conv} \sim 60$–70 d) are in reasonable agreement with semi-empirical values derived by Reiners, Basri & Browning (2009) but significantly lower than the predictions of Barnes & Kim (2010). The Rossby number is a crucial indicator of dynamo efficiency and is used in Section 7.7 for the description of the rotation–activity relation. The parameters $R_{\rm per}$ (column 6) and $S_{\rm ph}$ (column 7) are measures for the variability in the K2 light curve and are examined in this section. The amplitude of photometric variability associated with star-spots is determined by the temperature contrast between spotted and unspotted photosphere and by the spot coverage, and may therefore, to first approximation, be considered a measure for magnetic activity. Various photometric activity indices characterizing the amplitude of *Kepler* light curves have been used in the literature. Basri, Walkowicz & Reiners (2013) have introduced the range of variability between the 5th and 95th percentile of the observed flux values, $R_{\rm var}$. This definition is meant to remove the influence of flares which are occasional events involving only a small fraction of a given rotational cycle. To further reduce the influence of outliers, we follow the modified definition of

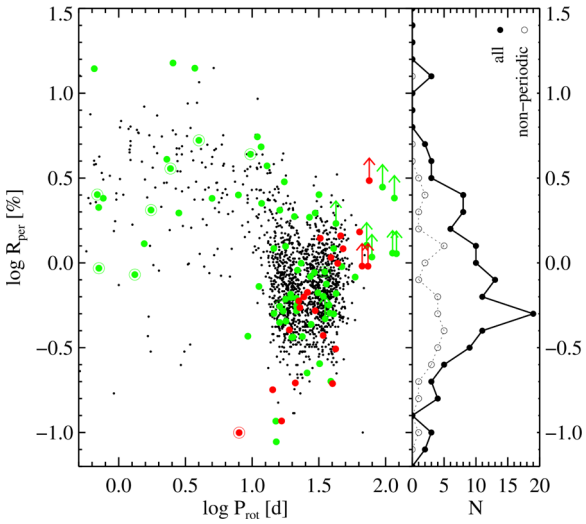

Figure 11. Period versus amplitude for the K2 Superblink M dwarf sample (large, coloured circles) compared to the *Kepler* field M dwarfs from (McQuillan et al. 2013, small, black dots). For our K2 sample, we distinguish reliable periods (green) and questionable periods (red). Banner on the right: histogram of $R_{\rm per}$ for the full K2 Superblink star sample (solid line) and for the subsample classified as non-periodic (flag 'N'). As in the other figures, binaries in our K2 Superblink sample are marked with large annuli.

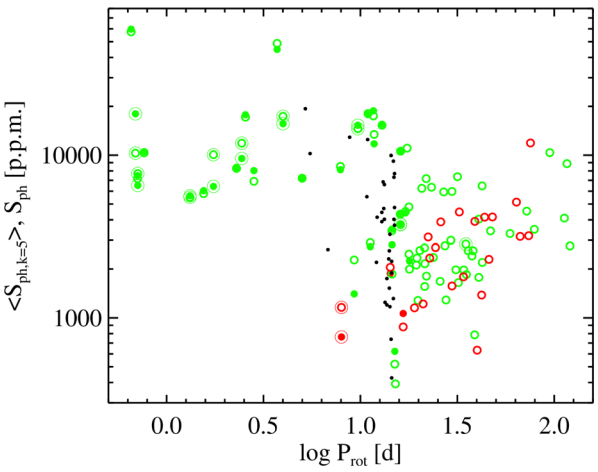

Figure 12. Magnetic activity indices defined by Mathur et al. (2014) versus period for the K2 Superblink star sample, compared to the subsample of 34 *Kepler* field M dwarfs studied by (Mathur et al. 2014, black dots). Green and red symbols represent periods flagged 'Y' and '?', respectively. Filled circles denote $\langle S_{\rm ph,k=5}\rangle$ values and open circles the $S_{\rm ph}$ values. See the text in Section 7.3 for details on the definition of these indices. Large annuli mark binaries.

McQuillan et al. (2013): $R_{\rm per}$ is the mean of the $R_{\rm var}$ values measured individually on all observed rotation cycles, expressed in percent.

Since in the course of our flare analysis we produce light curves where flares and other outliers have been eliminated we could use those 'cleaned' light curves for the analysis of the rotational variability. This way we could avoid cutting the top and bottom 5 per cent of the data points. We compute the difference between the full amplitudes measured on the 'cleaned' light curves and the $R_{\rm per}$ values measured on the original light curves and find them to differ by $\sim$0.05 $\pm$ 0.05 dex in logarithmic space. This is negligible to the observed range of amplitudes. In order to enable a direct comparison to results from the literature, we prefer, therefore, to stick to the $R_{\rm per}$ values derived from the original light curves. In Fig. 11, we show the relation between $P_{\rm rot}$ and $R_{\rm per}$ for the K2 Superblink M stars compared to the much larger *Kepler* M dwarf sample of McQuillan et al. (2013). The distribution of the two samples is in good agreement. In particular, there is a clear trend for stars with shorter periods to have larger spot amplitudes. We examine this finding in more detail below.

Fig. 11 also illustrates the difference between our results and those of McQuillan et al. (2013) for the longest periods. (Note that all K2 Superblink stars with periods inferred from sine-fitting have only a lower limit to the variability amplitude $R_{\rm per}$.) One reason for the absence of long-period stars in McQuillan et al. (2013) could be the larger distance of the *Kepler* stars which results in lower sensitivity for small amplitudes, suggesting that *Kepler* can find periods only in the more active stars likely to be rotating faster. However, remarkably, the long-period stars in the K2 Superblink M star sample seem to have larger spot amplitudes than stars with lower periods (from $\sim$15 to 50 d). We recall again that we are able to detect such long periods only on stars with clear sine-like variation indicating the presence of a single dominating spot. Therefore, we can only speculate that stars with periods $\gtrsim$100 d and low spot amplitude may exist but their more diffuse spot patterns or changes on time-scales shorter than the rotation period yield a complex light curve. If so, one can expect these stars among the ones classified as non-periodic (flag 'N') by us. The bar on the right of Fig. 11 shows the distribution of $R_{\rm per}$ for all K2 Superblink M stars and for the subsample to which we could not assign a period. There is no clear preference of these latter ones towards small amplitudes, and the above consideration does not allow us to conclude on their periods. Constraining the range of spot amplitude of the slowest rotators should be a prime goal of future studies on larger samples. As described in Section 7.2, we find the longest periods exclusively in very low mass stars. Therefore, the change in the distribution of the $R_{\rm per}$ values for the slowest rotators – if truly existing – might be a mass-dependent effect rather than related to rotation.

Mathur et al. (2014) defined the STD of the full light curve, $S_{\rm ph}$, and $\langle S_{\rm ph,\,k}\rangle$, the mean of the STD computed for time intervals $k \cdot P_{\rm rot}$. They found that for increasing k the index $\langle S_{\rm ph,k}\rangle$ approaches $S_{\rm ph}$. This way they were able to show that roughly after five rotation cycles ($k = 5$) the full range of flux variation is reached, and they recommend $\langle S_{\rm ph,k=5}\rangle$ as measure of the global evolution of the variability. We compute $S_{\rm ph}$ and $\langle S_{\rm ph,k=5}\rangle$ for the K2 Superblink M stars and show the results in Fig. 12 versus the rotation periods; filled circles represent $\langle S_{\rm ph,k=5}\rangle$ and open circles mark $S_{\rm ph}$. The sample studied by Mathur et al. (2014) is also displayed (black dots for their $\langle S_{\rm ph,k=5}\rangle$ values). That sample consists of 34 *Kepler* M stars with 15 Quarters of continuous observations and $P_{\rm rot} < 15$ d from the *Kepler* study of McQuillan et al. (2013). Our sample improves the period coverage especially for $P \lesssim 12$ d. The fact that there are no very fast rotators in the sample studied by Mathur et al. (2014) is probably a bias related to their sample selection. We find that stars with short periods have systematically larger $\langle S_{\rm ph,k=5}\rangle$ index than stars with $P \gtrsim 10$ d. The upper boundary of 15 d for the periods in the Mathur et al. (2014) sample is imposed by their requirement of covering at least five cycles. However, as explained above there is no dramatic difference between $\langle S_{\rm ph,k=5}\rangle$ and $S_{\rm ph}$ for a given star. We verify this on the K2 Superblink M star sample by showing as open circles their values $S_{\rm ph}$. The advantage of $S_{\rm ph}$ is that we can include in Fig. 12 the stars with $P > 1/5 \cdot \Delta t$. We can see that the pattern over the whole period range is very similar to that of Fig. 11, i.e. both spot amplitude and STD of the light curve show a

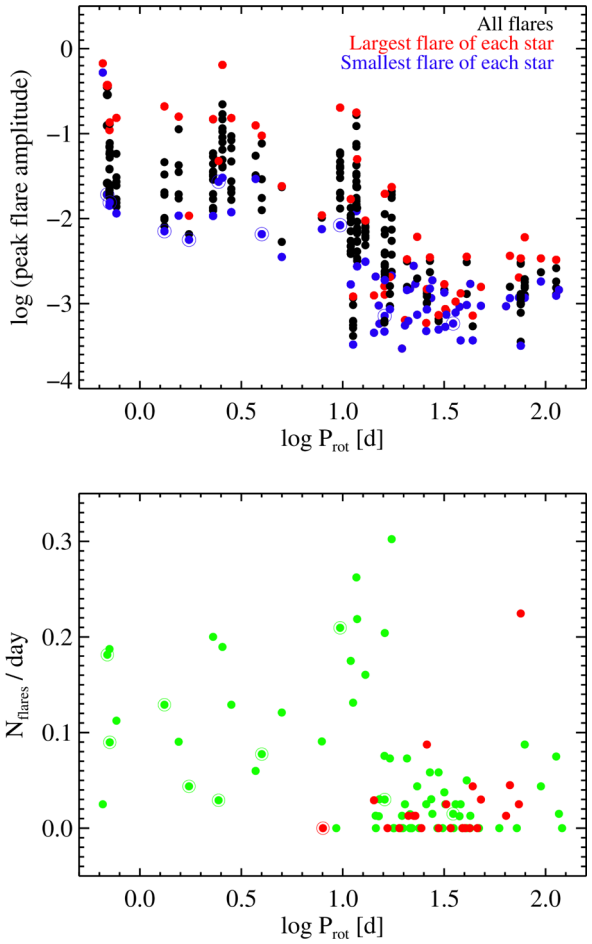

Figure 13. Top – flare amplitude versus rotation period: all flares are shown and the range of flare amplitudes for a given star is made evident by marking the largest and smallest flare on each star with different colours, red and blue, respectively. Bottom - flare frequency versus rotation period: each star is represented once. Binaries are highlighted in both panels with annuli.

dependence on rotation rate which seems to divide the stars in two groups above and below $P \sim 10$–12 d.

7.4 Activity diagnostics related to flares in K2 light curves

Our separate analysis of flares and rotation in the K2 light curves enables us to relate flare activity to star-spot activity. Fig. 13 shows the peak amplitudes of all flares defined with respect to the flattened K2 light curve (top panel) and the flare frequency of all stars (bottom panel) as function of the rotation period. A clear transition takes place near $P_{rot} \sim 10$ d, analogous to the case of the spot activity measures discussed in Section 7.3. While the absence of small flares in fast rotators is determined by the noise level in the flattened light curve (see Fig. 6), there is no bias against the detection of large flares in slowly rotating stars. Note that our algorithm has lower flare detection sensitivity for events on fast-rotating stars because the presence of flares itself impacts on the quality of the smoothing process used to identify the flares. Therefore, especially for the stars with short periods, the number of flares observed per day (N_{flares}/day) may represent a lower limit to the actual flare frequency.

Considering the limitations of the K2 LC data for flare statistics (see discussion in Section 4.2), we do not put much weight on the absolute numbers we derive for the flare rates. However, our results

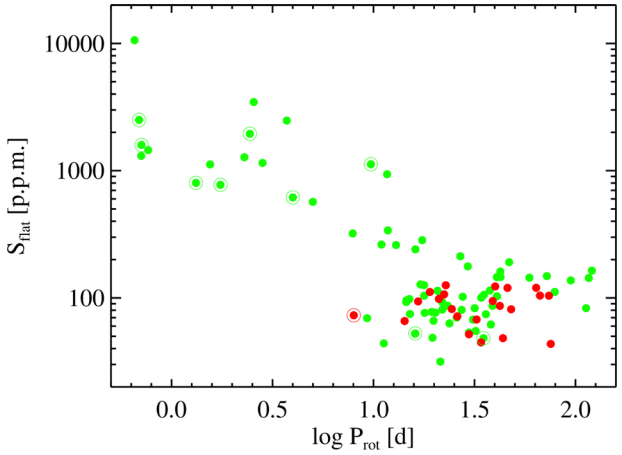

Figure 14. STD of the flattened light curve excluding the outliers, as in Fig. 6, shown here versus rotation period. Green symbols (period flag 'Y'), red symbols (period flag '?'). The clear transition between fast and slowly rotating stars indicates that for fast rotators the origin of this 'noise' has an astrophysical component. Binaries are highlighted with annuli.

are in very good agreement with a dedicated M dwarf flare study based on SC (1 min) *Kepler* light curves. In particular, for the fast rotators the range we show in Fig. 13 for the peak flare amplitudes (∼0.01–0.5) and for the number of flares per day (∼0.05–0.2), are similar to the numbers obtained by Hawley et al. (2014) for the active M star GJ 1243 if only flares with duration of more than 1 h are considered from that work.

7.5 Residual activity in K2 light curves

Above we have shown that both the spot cycle amplitude and the flares display a distinct behaviour with rotation period. Here, we examine the STD of the 'flattened' light curves, S_{flat}. As described in Section 4.3, when measured without considering the outliers, this parameter represents a measure for the noise after removal of the rotation cycle and of the flares. We notice a marked trend of S_{flat} with the rotation period (Fig. 14). A dependence of the noise level on the brightness of the star is expected and demonstrated in Fig. 6, where the lower envelope of the distribution increases towards fainter K_p magnitude. However, the difference between the S_{flat} values seen for slow and fast rotators in Fig. 14 is clearly unrelated to this effect as there is no clustering of stars with large S_{flat} (and fast rotation) at bright magnitudes in Fig. 6. The evidently bimodal distribution with rapid rotators showing larger values of S_{flat}, therefore suggests that there is a contribution to the 'noise' in the K2 photometry that is astrophysical in origin.

The similarity of the period dependence seen in S_{flat} (Fig. 14), the spot cycle (Figs 11 and 12) and the flares (Fig. 13) may indicate that the 'noise' in the fastest rotators could be caused by unresolved spot or flare activity. Many small flares, so-called nano-flares, as well as many small and/or rapidly evolving spots can produce a seemingly stochastic signal. These astrophysical noise sources seem to be limited to fast rotators, while for slow rotators the spot contrast drops below a constant minimum level of the variability which might be identified as the photometric precision (see Section 4.3).

7.6 Photometric activity and binarity

In the relations between various activity indicators and rotation period presented in the previous sections, binary stars that have a

possible contribution to the rotational signal from the unresolved companion star are highlighted. Strikingly, the binaries are mostly associated with rotation periods below the transition between fast and slow regimes that we have identified. In Fig. 14, this could be taken as evidence that the presence of a companion increases the noise in the K2 light curve. On the other hand, we have argued above that the coincidence of the bimodality in $S_{\rm flat}$, spot and flare signatures with $P_{\rm rot}$ points at a fundamental transition taking place in these stars. We may speculate that binarity is responsible for the observed dichotomy, e.g. by spinning up the star through tidal interaction or by reducing angular momentum loss. The binary fraction (*BF*) for the fast rotators ($P_{\rm rot} < 10$ d) is 8/19, i.e. 8 stars out of 19 are known binaries. For slow rotators ($P_{\rm rot} > 10$ d) the *BF* is 2/78. We calculate the 95 per cent confidence levels for a binomial distribution and find the two samples to be significantly different: $BF_{\rm fast} = 0.42^{+0.67}_{-0.20}$ and $BF_{\rm slow} = 0.03^{+0.09}_{-0.00}$. That said, we caution that no systematic and homogeneous search for multiplicity was done for these stars and our literature compilation (Section B) may be incomplete.

7.7 The X-ray and UV activity–rotation relation

The activity–rotation relation is traditionally expressed using X-rays, Ca II H&K and Hα emission as activity indicators. Measurements of these diagnostics have historically been easiest to achieve (Pallavicini et al. 1981; Noyes et al. 1984). Yet, as described in Section 1, the dependence between magnetic activity and rotation has remained poorly constrained for M stars. In Fig. 15, we present an updated view using the X-ray data extracted from the archives and the newly derived rotation periods from K2. We also add here, to our knowledge for the first time for field M stars, UV emission as diagnostic of chromospheric activity in conjunction with photometric rotation periods.

All but two of the 26 K2 Superblink stars with X-ray detection have reliable rotation period measurement (flag 'Y'). The first exception is EPIC-206019392 for which we find through sine-fitting a period of ∼75 d. While there are no doubts on a periodic spot-modulation, the slight deviations of its light curve from a sinusoidal make the value for the period uncertain (therefore flagged '?' in Table 2). For the other case, EPIC-210500368, we cannot identify a dominating period, yet the light curve shows a long-term trend superposed on a variability with a time-scale of ∼10 d. Among the NUV detections, we could establish the rotation period for 78 per cent (32/41), and 46 per cent (19/41) of them have a 'reliable' period. 9 of 11 FUV detected stars have a period measurement, of which 7 are flagged 'reliable'.

The parameters which best describe the connection between activity and rotation are still a matter of debate (Reiners, Schüssler & Passegger 2014). We provide here plots for luminosity versus rotation period (left-hand panels of Fig. 15) and for activity index $L_{\rm i}/L_{\rm bol}$ with $i = NUV, FUV, X$ versus Rossby number (right-hand panels). First, it is clear that there is a decrease of the activity levels in all three diagnostics (NUV, FUV, X-rays) for the slowest rotators. While the sample of M stars with FUV detection and rotation period measurement is still very small, a division in a saturated and a correlated regime, historically termed the 'linear' regime, can be seen in the relations involving NUV and X-ray emission. The X-ray–rotation relation is still poorly populated for slow rotators, and the turn-over point and the slope of the decaying part of the relation cannot be well constrained with the current sample. Interestingly, for the NUV emission the situation is reversed, in a sense that more stars with NUV detection are found among slow rotators. In terms of luminosity NUV saturation seems to hold up to periods of ∼40 d, way beyond the critical period of ∼10 d identified to represent a transition in the behaviour of optical activity indicators extracted from the K2 light curves (see Sections 7.3 and 7.4). On the other hand, the $L'_{\rm NUV}/L_{\rm bol}$ values are slightly decreased with respect to the levels of the fastest rotators, and the active stars around an ∼30–40 d period are all late-K to early-M stars. We also caution that a large fraction of the slowly rotating NUV detected stars have periods that we flagged as less reliable (red symbols in Fig. 15).

In order to highlight eventual differences emerging at the fully convective transition, we divide the stars in Fig. 15 into three SpT groups represented by different plotting symbols. As far as the X-ray emission is concerned, the two order of magnitude scatter in the saturated part of the $L_{\rm x}$ versus $P_{\rm rot}$ relation is clearly determined by the SpT distribution, with cooler stars having lower X-ray luminosities for given period. This is a consequence of the mass dependence of X-ray luminosity, and was already seen by Pizzolato et al. (2003) for coarser bins of stellar mass representing an SpT range from G to M. We have overplotted in the bottom panels of Fig. 15 the relation derived by Pizzolato et al. (2003) for their lowest mass bin, $M = 0.22$–$0.60\,{\rm M}_{\odot}$ (corresponding to SpT earlier than M2). It must be noted that in Pizzolato et al. (2003) the linear regime was populated by only two stars of their sample and the saturated regime was dominated by upper limits to $P_{\rm rot}$ which were estimated from $v \sin i$ measurements. Therefore, even our still limited K2 sample constitutes a significant step forward in constraining the X-ray–rotation relation of M dwarfs.

We determine the saturation level for all X-ray detections with $P_{\rm rot} < 10$ d in the three SpT bins K7–M2, M3–M4, and M5–M6 and for the whole sample with SpT from K7 to M6. The results are summarized in Table 5. If we select the K2 Superblink M star subsample in the same mass range studied by Pizzolato et al. (2003, $M = 0.22$–$0.60\,{\rm M}_{\odot}$), we derive saturation levels of $\log L_{\rm x,\,sat}\,[{\rm erg\,s^{-1}}] = 28.5 \pm 0.5$ and $\log(L_{\rm x,\,sat}/L_{\rm bol}) = -3.3 \pm 0.4$, within the uncertainties compatible with their results. We confirm results of previous studies that the saturation level for a sample with mixed SpT converges to a much narrower distribution if $\log(L_{\rm x}/L_{\rm bol})$ is used as activity diagnostic (see Fig. 15 and last line in Table 5). There is marginal evidence for the very low-mass stars (SpT M5–M6) to be underluminous with respect to this level. However, this assertion is not yet statistically sound according to the spread of the data (see STD in Table 5) and two-sample tests carried out with ASURV (Feigelson & Nelson 1985) indicate that the $\log(L_{\rm x}/L_{\rm bol})$ values of the three SpT subgroups may be drawn from the same parent distributions (p-values >10 per cent). It has been widely acknowledged that the activity levels show a drop for late-M dwarfs (e.g. West et al. 2008; Reiners et al. 2012), but an investigation of whether and how this is related to $P_{\rm rot}$ has come into reach only now with the large number of periods that can be obtained from planet transit search projects. Using rotation periods from the MEarth programme, West et al. (2015) showed that the average $L_{{\rm H}\alpha}/L_{\rm bol}$ ratio for fast rotators ($P_{\rm rot} < 10$–20 d) decreases by a factor 2 for late-M dwarfs (SpT M5–M8) compared to early-M dwarfs (SpT M1–M4). Whether a distinct regime exists in which Hα activity correlates with $P_{\rm rot}$ could not be established in that study. The X-ray and UV detections we present in this paper also do not adequately sample the regime of long periods. We refrain here from fitting that part of the rotation–activity relation because our upcoming *Chandra* observations together with the larger sample of periods that will be available for Superblink M stars at the end of the K2 mission will put us in a much better position to address this issue.

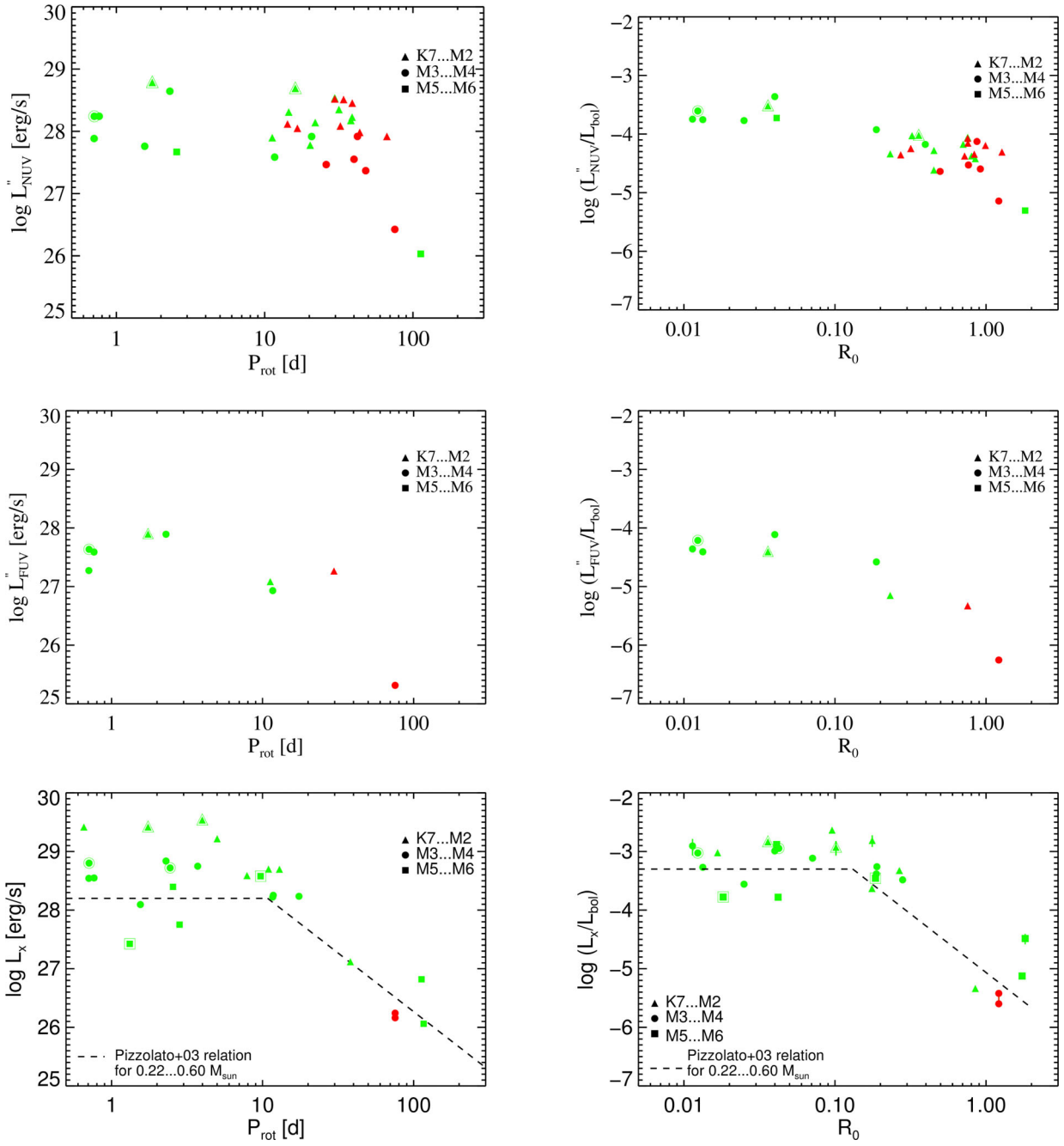

Figure 15. K2 rotation periods combined with archival NUV (top), FUV (middle) and X-ray (bottom) data for the campaign C0–C4 Superblink M stars. In the left-hand panels, luminosities versus rotation period, in the right-hand panels activity indices versus Rossby number. Periods flagged '?' are shown in red, unresolved binaries are represented with large annuli.

7.8 Activity and rotation of planet host stars

Being bright and nearby, the K2 Superblink stars have special importance for planet search studies. In fact, at the time of writing of this paper two of our targets already have confirmed planets discovered by the K2 mission. K2–3 is a system comprising three super-Earths confirmed through RV monitoring, with the outer planet orbiting close to the inner edge of the habitable zone (EPIC-201367065 observed in campaign C 1); see Crossfield et al. (2015) and Almenara et al. (2015). K2-18 (EPIC-201912552, also observed in C 1) has a $\sim$2 $R_\oplus$ planet which was estimated to receive 94 $\pm$ 21 per cent of the Earth's insolation (Montet et al. 2015). Both host stars are prime targets for characterization studies of the planetary atmospheres

Table 5. X-ray saturation level for M dwarfs determined for X-ray detected stars with $P_{\rm rot} < 10$ d.

SpT	$N\star$	$\log L_{\rm x,\,sat}$ (erg s^{-1})	$\log (L_{\rm x,\,sat}/L_{\rm bol})$
K7–M2	5	29.2 $\pm$ 0.4	-3.0 ± 0.4
M3–M4	7	28.6 $\pm$ 0.3	-3.1 ± 0.2
M5–M6	4	27.9 $\pm$ 0.5	-3.5 ± 0.4
K7–M6	16	28.7 $\pm$ 0.6	-3.2 ± 0.4

through transit spectroscopy. Thus, the analysis of their stellar activity is a necessary step towards a global physical description of these systems.

Another two stars from our K2 Superblink sample have planet candidates presented by Vanderburg et al. (2016). These objects are not yet verified by RV measurements. Our analysis shows that for both systems the stellar rotation is not synchronized with the planet orbital period ($P_{\rm orb} = 1.8$ d and $P_{\rm rot} = 17.9$ d for EPIC-203099398 and $P_{\rm orb} = 14.6$ d and $P_{\rm rot} = 22.8$ d for EPIC-205489894, respectively).

8 DISCUSSION

We present here the first full flare and rotation period analysis for a statistical sample of K2 light curves. Our target list of bright and nearby M dwarfs represents a benchmark sample for exoplanet studies and will be thoroughly characterized by *Gaia* in the near future. Knowledge of the magnetic activity of these stars is of paramount importance given the potential impact it has on exoplanets. At the moment a planet is detected, the high-energy emission of any given K2 target and its variability becomes a prime interest (see e.g. Schlieder et al. 2016, for a recent example). With the study presented here and future analogous work on the remaining K2 campaigns we anticipate such concerns.

Our primary aim here is to understand the stellar dynamo and angular momentum evolution at the low-mass end of the stellar sequence through a study of relations between magnetic activity and rotation. We characterize activity with a multiwavelength approach involving archival X-ray and UV observations as well as parameters extracted directly from the K2 light curves which describe spot amplitudes and flares. This way we provide a stratified picture of magnetic activity from the corona over the chromosphere down to the photosphere. To our knowledge this is the first time that the link with photometrically determined rotation periods is made for a well-defined sample of M stars over such a broad range of activity diagnostics. Yet, as of today, only about 25 per cent of the M dwarfs with K2 rotation periods have a meaningful X-ray measurement, and this percentage is even lower for the NUV and FUV bands. Dedicated X-ray and UV follow-up of these objects can provide the ultimate constraints on the M dwarf rotation–activity relation.

Visual inspection of the K2 light curves shows that there is not a single non-variable star in this sample of 134 M dwarfs. We can constrain rotation periods in 73 per cent of them. The distribution of rotation periods we find for our sample is in general agreement with studies from the main *Kepler* mission with much larger but less well-characterized M star samples (McQuillan et al. 2013, 2014). Contrary to these studies we find long periods up to ∼100 d, thanks to our complementary use of direct sine-fitting as period detection method next to ACF and LS periodograms. We detect such long periods only in the lowest mass stars ($M \leq 0.4\,{\rm M}_{\odot}$). In this respect, our results resemble those obtained by Irwin et al. (2011) and Newton et al. (2016) based on the MEarth programme where sine-fitting yielded many long periods. However, unlike that project our sample includes also early-M type stars and, therefore, it has allowed us to establish that there is a dearth of long-period detections in early-M dwarfs. Until corroborated by a larger sample, we can only speculate whether this is due to the evolution of spin-down history across the stellar mass sequence or whether it results from a change in spot pattern and related changes in the detection capabilities for the associated periods.

The low cadence of the K2 light curves allows us to detect only the flares with duration ≥1 h, and due to this sparse sampling we refrain from a detailed analysis of flare statistics. Yet, we find an unprecedented link between flares and stellar rotation. The distribution of flare amplitudes and flare frequencies shows a clear transition at $P_{\rm rot} \sim 10$ d. The large flares seen in stars rotating faster than this boundary are absent in slow rotators although there is no detection bias against them. The smaller flares on slow rotators have no counterparts in the fast rotators but such events – if present – would likely be undetectable. We find the same bimodality between fast and slow rotators in the noise level ($S_{\rm flat}$) of the residual light curves after the rotational signal, flares and other 'outliers' are subtracted off. The residual variability seen in the fast rotators is significantly and systematically larger than in the slow rotators with a dividing line at $P_{\rm rot} \sim 10$ d. These new findings can now be added to the rotation-dependence of the spot cycle amplitude ($R_{\rm per}$) already known from the above-mentioned *Kepler* studies. A cut exists at the same period of ∼10 d with faster rotating stars showing larger amplitudes of the rotation cycle. These similarities lead us to speculate that the 'noise' (i.e. the high values of $S_{\rm flat}$) seen in the fast rotators is produced by smaller or fast-changing spots or by microflares that cause seemingly random variations.

The observed dichotomy in photometric activity levels between fast and slow rotators points to a rotation-dependent rapid transition in the magnetic properties of the photospheres in M dwarfs. In fact, an analogous sharp transition is observed in some numerical dynamo models at $R_{0,1} \sim 0.1$, where $R_{0,1}$ is the 'local Rossby number' (e.g. Schrinner, Petitdemange & Dormy 2012). Assuming this theoretical Rossby number corresponds with its empirical definition (see Section 7.3), this corresponds roughly to our observed critical period of ∼10 d. In the simulations, for $R_{0,1} > 0.1$ (slow rotators) the dipolar component of the dynamo collapses giving way to a multipolar dynamo regime. Gastine et al. (2013) have compared these predictions to the magnetic field structure inferred from ZDI of M dwarfs. Such observations are time-consuming and they require substantial modelling effort, and the samples tend to be biased towards fast rotators. When interpreted in terms of the above-mentioned models, our results suggest photometric rotation and activity measures as a new window for observational studies of dynamo flavours in M dwarfs. However, it must be questioned whether these diagnostics, which represent activity on the stellar surface, are sensitive to the large-scale component of the magnetic field.

The transition seen in star-spots and white-light flares also corresponds approximately to the period where previous studies of the X-ray–rotation relation have placed the transition from the 'saturated' to the 'linear' regime (e.g. Pizzolato et al. 2003). Different explanations have been put forth for this finding involving the filling factor for active regions, the size of coronal loops or the dynamo mechanism. Observationally, those studies have so far shown clear rotation–activity trends only for higher mass stars. We extend the X-ray–rotation relation here to well-studied M stars. With our data set we can, for the first time, refine the study of X-ray emission from field M dwarfs in the saturated regime (fast rotation) in bins spanning spectral subclasses and we find a continuous decrease of the saturation level $L_{\rm x}$ towards later SpT which can be understood in terms of the mass dependence of X-ray luminosity. The tentative evidence that the saturated stars in the coolest mass bin (SpT M5–M6) have lower $L_{\rm x}/L_{\rm bol}$ than the K7–M4 type stars is not statistically solid yet. If confirmed on a larger sample this might represent a change at the fully convective transition, whether due to magnetic field strength or structure, or its coupling to rotation (i.e. the stellar dynamo). It is by now well established that there is a sharp drop of X-ray and Hα activity at late-M SpT (∼ M7–M8; e.g. West et al. 2008; Cook, Williams & Berger 2014) but for mid-M SpT, so far, X-ray studies have not been resolved in both $P_{\rm rot}$ and SpT space together. If, e.g. late-M stars remain saturated up to longer periods,

the decrease of the saturation level may go unnoticed in samples mixing the whole rotational distribution.

We add in this study the first assessment of a link between rotation and chromospheric UV emission in M stars. Similar to the archival X-ray data, the UV data (from the *GALEX* mission) covers only a fraction of the K2 sample. A curious wealth of stars with high UV emission levels and long periods is seen that seems to be in contrast with the findings regarding all other activity indicators discussed in this work.

Finally, our archive search for evidence of multiplicity in our targets raises an interesting point about the possible influence of multiplicity on rotation and activity levels. We find a high incidence of binarity in the group of fast rotators below the critical period at which magnetic activity apparently transitions to a lower level. The difference between the *BF* of fast and slow rotators is statistically significant. Given the rather large binary separations (of tens to hundreds of astronomical units) this is puzzling because no tidal interaction is expected for such wide systems. Nevertheless, we can speculate about a possible causal connection between binarity and rotation level. It is well established that wide companions accelerate the evolution of pre-main-sequence discs (e.g. Kraus et al. 2012). Shorter disc lifetimes translate into a shorter period of star–disc interaction and, hence, one may expect higher initial rotation rates on the main sequence for binary stars (Herbst & Mundt 2005). As a result, it may take binaries longer to spin-down. Alternatively, we could be seeing the mass-dependence of magnetic braking. With our low-number statistics, we cannot draw any firm conclusions. Note, however, that a relation between fast rotation and binarity, independent of stellar mass, was also found in a recent K2 study of the Hyades (Douglas et al. 2016).

9 SUMMARY AND OUTLOOK

From a joint rotation and multiwavelength activity and variability study of nearby M dwarfs observed in K2 campaigns C0–C4 we infer a critical period of ∼10 d at which photometric star-spot and flare activity undergoes a dramatic change. This transition is coincident with the break separating saturated from 'linear' regime seen in traditional studies of the rotation–activity relation probing higher atmospheric layers (e.g. the corona through X-rays or the chromosphere through Hα emission). We present here an updated view of the X-ray–rotation relation for M dwarfs. The sample analysed in this work has strongly increased the known number of long-period M dwarfs in the X-ray–rotation relation. Nevertheless, at present there is not enough sensitive data in the X-ray archives to constrain the X-ray–rotation relation for periods beyond ∼10 d. A key questions is now whether the coronal emission of M dwarfs displays a break-point analogous to the optical photometric activity tracers or whether there is a continuous decrease of activity as seen in FGK stars. This problem will be addressed in the near future with upcoming *Chandra* observations in which we sample the whole observed K2 rotation period distribution. We will also further examine the UV–rotation relation in the larger M dwarf sample that will be available at the end of the K2 mission. Moreover, in that larger sample we intend to search for a possible mass dependence of the rotation–activity relation within the M spectral sequence. A systematic assessment of multiplicity for these nearby M stars with *Gaia* will also be useful for examining the influence of a companion star on rotation and activity levels.

The observed dichotomy between fast and slow rotators in terms of their magnetic activity level might have interesting consequences for habitability of planets near M stars being fried by flares and high-energy radiation until they have spun down to around 10 d. The time-scale for this process is as yet poorly constrained but certainly on the order of giga years, and it becomes longer the lower the mass of the star (West et al. 2008). Segura et al. (2010) found in models based on AD Leo that UV flares do not strongly affect planet chemistry but the accumulated effect of the exposure to strong flaring over most of the planet's lifetime has not been studied so far.

ACKNOWLEDGEMENTS

We would especially like to thank A. Vanderburg for his public release of the analysed K2 light curves, upon which much of the present work is based. We thank the anonymous referee for a very careful reading of our manuscript. This research has made use of the VizieR catalogue access tool, and the 'Aladin sky atlas', both developed at CDS, Strasbourg Observatory, France.

REFERENCES

Allard F., Hauschildt P. H., Alexander D. R., Tamanai A., Schweitzer A., 2001, ApJ, 556, 357
Almenara J. M. et al., 2015, A&A, 581, L7
Andersen J. M., Korhonen H., 2015, MNRAS, 448, 3053
Angus R., Foreman-Mackey D., Johnson J. A., 2016, ApJ, 818, 109
Armstrong D. J. et al., 2015, A&A, 579, A19
Barnes S. A., Kim Y.-C., 2010, ApJ, 721, 675
Basri G., Walkowicz L. M., Reiners A., 2013, ApJ, 769, 37
Beuzit J.-L. et al., 2004, A&A, 425, 997
Bianchi L., 2009, Astrophys. Space Sci., 320, 11
Bianchi L., Herald J., Efremova B., Girardi L., Zabot A., Marigo P., Conti A., Shiao B., 2011, Astrophys. Space Sci., 335, 161
Borucki W. J. et al., 2010, Science, 327, 977
Bouvier J., Matt S. P., Mohanty S., Scholz A., Stassun K. G., Zanni C., 2014, in Beuther H., Klessen R. S., Dullemond C. P., Henning T., eds, Protostars and Planets VI. Univ. Arizona Press, Tucson, AZ, p. 433
Bowler B. P. et al., 2015, ApJ, 806, 62
Brown T. M., Latham D. W., Everett M. E., Esquerdo G. A., 2011, AJ, 142, 112
Browning M. K., Basri G., Marcy G. W., West A. A., Zhang J., 2010, AJ, 139, 504
Chabrier G., Küker M., 2006, A&A, 446, 1027
Cook B. A., Williams P. K. G., Berger E., 2014, ApJ, 785, 10
Cranmer S. R., Saar S. H., 2011, ApJ, 741, 54
Crespo-Chacón I., Montes D., García-Alvarez D., Fernández-Figueroa M. J., López-Santiago J., Foing B. H., 2006, A&A, 452, 987
Crossfield I. J. M. et al., 2015, ApJ, 804, 10
Davenport J. R. A. et al., 2014, ApJ, 797, 122
Delorme P., Collier Cameron A., Hebb L., Rostron J., Lister T. A., Norton A. J., Pollacco D., West R. G., 2011, MNRAS, 413, 2218
Dittmann J. A., Irwin J. M., Charbonneau D., Berta-Thompson Z. K., 2014, ApJ, 784, 156
Donati J.-F., Landstreet J. D., 2009, ARA&A, 47, 333
Donati J.-F. et al., 2015, MNRAS, 453, 3706
Douglas S. T., Agüeros M. A., Covey K. R., Cargile P. A., Barclay T., Cody A., Howell S. B., Kopytova T., 2016, ApJ, 822, 47
Durney B. R., De Young D. S., Roxburgh I. W., 1993, Sol. Phys., 145, 207
Feigelson E. D., Nelson P. I., 1985, ApJ, 293, 192
Foreman-Mackey D., Montet B. T., Hogg D. W., Morton T. D., Wang D., Schölkopf B., 2015, ApJ, 806, 215
France K. et al., 2013, ApJ, 763, 149
Gallet F., Bouvier J., 2013, A&A, 556, A36
Gastine T., Morin J., Duarte L., Reiners A., Christensen U. R., Wicht J., 2013, A&A, 549, L5
Gliese W., Jahreiß H., 1991, in Brotzmann L. E., Gesser S. E. (eds), On: The Astronomical Data Center CD-ROM: Selected Astronomical Catalogs, Vol. I. Goddard Space Flight Center, MD
Guenther E. W., Paulson D. B., Cochran W. D., Patience J., Hatzes A. P., Macintosh B., 2005, A&A, 442, 1031

Hartman J. D., Bakos G. Á., Kovács G., Noyes R. W., 2010, MNRAS, 408, 475
Hartman J. D., Bakos G. Á., Noyes R. W., Sipőcz B., Kovács G., Mazeh T., Shporer A., Pál A., 2011, AJ, 141, 166
Hawley S. L., Davenport J. R. A., Kowalski A. F., Wisniewski J. P., Hebb L., Deitrick R., Hilton E. J., 2014, ApJ, 797, 121
Henden A., Munari U., 2014, Contrib. Astron. Obs. Skalnate Pleso, 43, 518
Henden A. A., Templeton M., Terrell D., Smith T. C., Levine S., Welch D., 2016, VizieR Online Data Catalog, 2336
Herbst W., Mundt R., 2005, ApJ, 633, 967
Howell S. B. et al., 2014, PASP, 126, 398
Irwin J., Berta Z. K., Burke C. J., Charbonneau D., Nutzman P., West A. A., Falco E. E., 2011, ApJ, 727, 56
Jones E. et al., 2001, SciPy: Open Source Scientific Tools for Python. Available at: https://www.scipy.org/citing.html
Kawaler S. D., 1988, ApJ, 333, 236
Kiraga M., 2012, Acta Astron., 62, 67
Kopparapu R. K., 2013, ApJ, 767, L8
Kosovichev A. G., de Gouveia Dal Pino E., Yan Y., 2013, IAU Symp. 294, Solar and Astrophysical Dynamos and Magnetic Activity
Kraus A. L., Ireland M. J., Hillenbrand L. A., Martinache F., 2012, ApJ, 745, 19
Lépine S., Gaidos E., 2011, AJ, 142, 138
Lépine S., Hilton E. J., Mann A. W., Wilde M., Rojas-Ayala B., Cruz K. L., Gaidos E., 2013, AJ, 145, 102
Luger R., Barnes R., Lopez E., Fortney J., Jackson B., Meadows V., 2015, Astrobiology, 15, 57
Lurie J. C., Davenport J. R. A., Hawley S. L., Wilkinson T. D., Wisniewski J. P., Kowalski A. F., Hebb L., 2015, ApJ, 800, 95
McCarthy C., Zuckerman B., Becklin E. E., 2001, AJ, 121, 3259
McQuillan A., Aigrain S., Mazeh T., 2013, MNRAS, 432, 1203
McQuillan A., Mazeh T., Aigrain S., 2014, ApJS, 211, 24
Mann A. W., Feiden G. A., Gaidos E., Boyajian T., von Braun K., 2015, ApJ, 804, 64
Mann A. W., Feiden G. A., Gaidos E., Boyajian T., von Braun K., 2016, ApJ, 819, 87
Mathur S., Salabert D., García R. A., Ceillier T., 2014, J. Space Weather Space Clim., 4, A15
Matt S. P., Brun A. S., Baraffe I., Bouvier J., Chabrier G., 2015, ApJ, 799, L23
Montet B. T. et al., 2015, ApJ, 809, 25
Morin J. et al., 2008, MNRAS, 390, 567
Morin J., Donati J.-F., Petit P., Delfosse X., Forveille T., Jardine M. M., 2010, MNRAS, 407, 2269
Morrissey P. et al., 2005, ApJ, 619, L7
Morrissey P. et al., 2007, ApJS, 173, 682
Neuhäuser R., Sterzik M. F., Schmitt J. H. M. M., Wichmann R., Krautter J., 1995, A&A, 297, 391
Newton E. R., Charbonneau D., Irwin J., Berta-Thompson Z. K., Rojas-Ayala B., Covey K., Lloyd J. P., 2014, AJ, 147, 20
Newton E. R., Irwin J., Charbonneau D., Berta-Thompson Z. K., Dittmann J. A., West A. A., 2016, ApJ, 821, 93
Nielsen M. B., Gizon L., Schunker H., Karoff C., 2013, A&A, 557, L10
Noyes R. W., Hartmann L. W., Baliunas S. L., Duncan D. K., Vaughan A. H., 1984, ApJ, 279, 763
Pallavicini R., Golub L., Rosner R., Vaiana G. S., Ayres T., Linsky J. L., 1981, ApJ, 248, 279
Penz T., Micela G., 2008, A&A, 479, 579
Pfeffermann E., Briel U. G., Freyberg M. J., 2003, Nucl. Instrum. Methods Phys. Res. A, 515, 65
Pizzolato N., Maggio A., Micela G., Sciortino S., Ventura P., 2003, A&A, 397, 147
Press W. H., Rybicki G. B., 1989, ApJ, 338, 277
Ramsay G., Doyle J. G., Hakala P., Garcia-Alvarez D., Brooks A., Barclay T., Still M., 2013, MNRAS, 434, 2451
Rappaport S. et al., 2014, ApJ, 788, 114
Reid I. N. et al., 2004, AJ, 128, 463
Reiners A., Mohanty S., 2012, ApJ, 746, 43
Reiners A., Basri G., Browning M., 2009, ApJ, 692, 538
Reiners A., Joshi N., Goldman B., 2012, AJ, 143, 93
Reiners A., Schüssler M., Passegger V. M., 2014, ApJ, 794, 144
Rosen S. R. et al., 2016, A&A, 590, A1
Rugheimer S., Kaltenegger L., Segura A., Linsky J., Mohanty S., 2015, ApJ, 809, 57
Sanz-Forcada J., Micela G., 2002, A&A, 394, 653
Saxton R. D., Read A. M., Esquej P., Freyberg M. J., Altieri B., Bermejo D., 2008, A&A, 480, 611
Scargle J. D., 1982, ApJ, 263, 835
Schlieder J. E. et al., 2016, ApJ, 818, 87
Schrinner M., Petitdemange L., Dormy E., 2012, ApJ, 752, 121
Segura A., Kasting J. F., Meadows V., Cohen M., Scalo J., Crisp D., Butler R. A. H., Tinetti G., 2005, Astrobiology, 5, 706
Segura A., Walkowicz L. M., Meadows V., Kasting J., Hawley S., 2010, Astrobiology, 10, 751
Skumanich A., 1972, ApJ, 171, 565
Stassun K. G. et al., 2011, in Johns-Krull C., Browning M. K., West A. A., eds, ASP Conf. Ser. Vol. 448, 16th Cambridge Workshop on Cool Stars, Stellar Systems, and the Sun. Astron. Soc. Pac., San Francisco, p. 505
Stelzer B., Marino A., Micela G., López-Santiago J., Liefke C., 2013, MNRAS, 431, 2063
Vanderburg A., Johnson J. A., 2014, PASP, 126, 948
Vanderburg A. et al., 2016, ApJS, 222, 14
Vidotto A. A. et al., 2014, MNRAS, 441, 2361
Vilhu O., 1984, A&A, 133, 117
West A. A. et al., 2004, AJ, 128, 426
West A. A., Hawley S. L., Bochanski J. J., Covey K. R., Reid I. N., Dhital S., Hilton E. J., Masuda M., 2008, AJ, 135, 785
West A. A., Weisenburger K. L., Irwin J., Berta-Thompson Z. K., Charbonneau D., Dittmann J., Pineda J. S., 2015, ApJ, 812, 3
Wright N. J., Drake J. J., Mamajek E. E., Henry G. W., 2011, ApJ, 743, 48
Zacharias N., Finch C. T., Girard T. M., Henden A., Bartlett J. L., Monet D. G., Zacharias M. I., 2013, AJ, 145, 44

SUPPORTING INFORMATION

Additional Supporting Information may be found in the online version of this article.

Table 1. Target list for K2 Campaign C0–C4 with stellar parameters.
Table 2. Rotation and activity parameters derived from the K2 light curves.
Appendix A. Phase-folded light curves.
Figure A1. Folded K2 light curves with period flag 'Y' in Table 2.
Figure A2. Folded K2 light curves with period flag '?' in Table 2.
(http://www.mnras.oxfordjournals.org/lookup/suppl/doi:10.1093/mnras/stw1936/-/DC1).

Please note: Oxford University Press is not responsible for the content or functionality of any supporting materials supplied by the authors. Any queries (other than missing material) should be directed to the corresponding author for this article.

APPENDIX A: PHASE-FOLDED LIGHT CURVES

In the online materials, we present the phase-folded light curves for all periodic stars in two figures, one for periods flagged 'Y' (Fig. A1) and another one for periods flagged '?' (Fig. A2). For each star the light curve was folded with the 'adopted' period, i.e. either the LS period, the autocorrelation period (ACF) or the period from the sine-fit (SINE); see Section 4.4 for details.

APPENDIX B: SEARCH FOR BINARITY

We search all K2 Superblink stars for archival evidence of binarity. We proceed in several steps. First, we perform a visual inspection

Table B1. Companions possibly contaminating the K2 photometry.

EPIC ID	Campaign	Companion	Sep[a] (arcsec)	Epoch	J (mag)	Δ (mag)	Evidence for binarity plates	WDS	K2	Notes
202059188	C0	WDS 06102+2234	1.90	2012	–		x	x		1954 versus1997 plates: in 1997 the star was fully superposed with another object.
201909533	C1	WDS 11519+0731	SB	2013	–	–		x		Triple star studied by Bowler et al. (2015); primary is a spectroscopic binary with nearly equal mass components; it forms a common proper motion pair with an object of SpT M8V and $\Delta H = 5.4$ mag.
202571062	C2	WDS 16240−2911	6.20	2009	9.60			x		Alternative name UCAC4 305−091749
203124214	C2	WDS 16254−2710	2.80	2000	–	0.5		x	x	Magnitude difference from WDS; no reference found.
204976998	C2	UCAC4 351−084361	7.60	2000	11.25				x	
205467732	C2	WDS 16268−1724	0.50	2010	–	0.4		x		Magnitude difference from WDS; no reference found.
205952383	C3	2MASS 22362748−16172	7.00	2000	12.24				x	
206007536	C3	UCAC4 377−172716	6.40	2000	10.71				x	
206208968	C3	WDS 22334-0937	1.50	2010	–	0(J, K)		x		Binary resolved by McCarthy, Zuckerman & Becklin (2001) who report separation and magnitude difference.
206262223[b]	C3	UCAC4 406−139520	8.00	2012	9.46				x	Companion of EPIC-206262336.
	C3	WDS 22173−0847	0.70	2014	–	1.2(K)		x		Additional spectroscopic companion; separation and SpT (M7V) from WDS; magnitude difference from Beuzit et al. (2004).
	C3	UCAC4 406−139522	8.00	2012	9.02				x	Companion of EPIC-206262223 (see above).
206262336[b]	C3	WDS 22173−0847	2.60	2010	–			x		Additional companion; separation from WDS.
210613397	C4	WDS 03462+1710	14.3	2008	9.00			x	x	Alternative name UCAC4 536-007198. Companion is brighter and of earlier SpT (K4/5).
210651981	C4	WDS 04285+1742	1.60	2004	–	1.3(J)		x		Binary resolved by Guenther et al. (2005) who report separation and magnitude difference.

[a] 'SB' indicates spectroscopic binary.
[b] See the text in Appendix B on this quadrupel system.

of POSS1_RED and POSS2_RED photographic plates by using the online Digitized Sky Survey (DSS) and the interactive tools of Aladin. Epochs of each pair of plates are separated by up to ∼40 yr, with the most recent plates obtained in the 1990s. Comparison of the two epochs can help in identifying possible blends in the K2 photometry. Specifically, we examine if the targets significantly approached other stars due to their proper motion. Then, we search for photometric and astrometric information of each possible contaminant by matching the UCAC4 and 2MASS catalogues in Vizier. Taking into account that the K2 pixel scale is ∼4 arcsec pixel^{-1}, for those cases with possible blends we check the K2 imagettes and the photometric mask produced and used by A.Vanderburg in the reduction of the K2 data[10] to estimate visually the occurrence of blending and its significance. For each target, the inspected imagette represents the sum of all the single imagettes recorded by K2 during a campaign. From our experience such merged imagettes are usually affected by the shift on the sensor of the photometric centroid due to pointing drift of the telescope. The photometric masks are wide enough to take into account the drift of the centroids, making any quantitative analysis of blending with other astrophysical objects rather difficult and beyond the scope of this work. We also search the Washington Double Star catalogue (WDS) for information about binarity including subarcsec separations, which cannot be detected simply by visual inspection of the photographic plates or matching with other catalogues. For binaries in the WDS, we adopt the visual magnitude difference between the components indicated in the catalogue, when available and other photometric measurements were missing.

With this approach, we find evidence for a companion for 25 stars. However, many of the secondaries have a J magnitude which is more than 4 mag fainter than our target. These secondaries contribute at most a few per cent to the flux of the system. They are unlikely to be responsible for the observed rotational signal, and we do not consider them any further. We list the remaining potential companions in Table B1. These objects have either a J magnitude difference of <4 mag with respect to the corresponding K2 target, or a small separation according to the WDS catalogue without known photometry, or both. Next to an identifier for the putative companion (column 3) we provide the binary separation (column 4), the epoch to which it refers (column 5), the J magnitude or a magnitude difference between the two components according to the WDS (columns 6–7), and flags indicating how we identify it (through visual inspection of photographic plates, as entry in the WDS, or in the K2 imagette; columns 8–10). In a final 'Notes' column and in footnotes we add further explanations where needed.

The most important fact to note concerns the binary Gl 852 AB. Both stars are in our target list (EPIC-206262223 and EPIC-206262336) but they are clearly unresolved in A.Vanderburg's K2 pipeline. In fact, the light curves of both stars are identical because the aperture comprises an elongated object, clearly representing the two stars of the 8 arcsec binary. We also add a special note here on EPIC-204927969. Our inspection of the K2 imagette shows that the aperture used by Vanderburg includes other objects but our reconstruction of the light curve without the contaminated pixels proved that the rotational modulation is due to the target. Other possible contaminations to be taken serious regard the companions that have $J < 10$ mag. There are two such objects listed in Table B1. Another three K2 Superblink stars have companions with $J < 12.5$ mag which might contribute somewhat to the variability in the light curve. Further three multiples are presented in the literature, one spectroscopic binary and two close visual binaries. For the remaining objects in Table B1 we find no photometric measurements, and they are likely faint and may not influence the K2 light curves. All stars in Table B1 are flagged on the figures involving periods and activity measures from K2 data.

[10] https://www.cfa.harvard.edu/∼avanderb/k2.html

This paper has been typeset from a TEX/LATEX file prepared by the author.